3D Monte Carlo surface-atmosphere radiative transfer modelling with DART

Yingjie Wang, Nicolas Lauret, Omar Regaieg, Xuebo Yang, Jordan Guilleux, Eric Chavanon, Abdelaziz Kallel, Mustapha Moulana, Jérôme Colin, Olivier Hagolle, et al.

3D Monte Carlo surface-atmosphere radiative transfer modelling with DART

Yingjie Wang [a, *], Nicolas Lauret [a], Omar Regaieg [a, b], Xuebo Yang [c], Jordan Guilleux [a], Eric Chavanon [a], Abdelaziz Kallel [d], Mustapha Moulana [e], Jérôme Colin [a], Olivier Hagolle [f], Didier Ramon [e], Jean-Philippe Gastellu-Etchegorry [a]

[a] CESBIO, Université de Toulouse, CNES/CNRS/INRAE/IRD/UT3-Paul Sabatier, 18, Avenue Edouard Belin, 31401 Toulouse, France

[b] University of Bonn, Bonn, Germany

[c] Aerospace Information Research Institute, Chinese Academy of Sciences, Beijing 100094, China

[d] CRNS, ATMS, Sfax, Tunisia

[e] HYGEOS, 165 Avenue de Bretagne, Euratechnologies, Lille, France

[f] CNES, 18 avenue Edouard Belin, 31401 Toulouse, France

Correspondence to: Yingjie Wang (yingjie.wang@iut-tlse3.fr)

Research highlights:

New 3D Monte Carlo surface-atmosphere RT modelling in DART model.

A virtual Earth-Atmosphere laboratory for simulating the adjacency effect.

Study of the impact of the surface 3D structure on the adjacency effect.

Study of the adjacency effect contribution on radiance and albedo at TOC and TOA.

Abstract

Significant errors can arise if the adjacency effect (*i.e.*, the contribution of neighbouring pixels to the radiance of a pixel) is neglected in the interpretation of remote sensing images. For example, adjacency radiances can account for more than 30% of the signal at the top of the atmosphere (TOA) of a white sand-lined coastline (Bulgarelli and Zibordi, 2018). This paper shows that 3D radiative transfer (RT) modelling can quantify this phenomenon. It presents a new 3D Monte Carlo surface-atmosphere RT modelling in the DART RT model, and a resulting virtual 3D Earth-Atmosphere laboratory for accurate simulation of atmospheric RT, including the adjacency effect. It was first validated with the atmosphere model SMART-G for 2D scenes: relative difference is 0.20% in TOA directional reflectance of infinite black surface for solar zenith equal to 60°, and 0.03% in TOA nadir reflectance of a black disc inside infinite white Lambertian surface, for solar zenith equal to 0° and 30°. Then, the adjacency effect on the TOA radiance and TOA albedo of a 3D scene was studied for a circular city (radius 2 km) surrounded by a forest (dimension 10 km), for four Sentinel-2A bands (blue, green, red, near infrared). Its contribution to TOA nadir radiance reaches ~20% in the near infrared band, and increases with viewing zenith angle (VZA): ~60% if VZA = 80°. The 3D scene TOA albedo was calculated after adapting the DART Bidirectional Reflectance Factor (BRF) camera to simulate TOA radiance for all upward directions at any angular resolution. For Sentinel-2A's four bands, the adjacency effect influences the TOA albedo of the circular city by up to 10% for the green band and up to 27% for the near infrared band, well above the maximum uncertainty 5% usually required in land surface applications. The adjacency effect of the city neighbourhood 3D structure was studied by replacing it by a Lambertian surface with its albedo. The city nadir TOA radiance changed by up to 1.3% with very small change in TOA albedo (< 0.5%). This new modelling greatly improves DART potential for accurate simulation of atmospheric effects. It is in the DART version freely available for research and education (https://dart.omp.eu).

Key words

DART, Monte Carlo, Atmosphere, Adjacency effect, Radiative transfer

1 Introduction

From a remote sensing point of view, the adjacency effect is the part of the measured signal due to land surface elements outside the instantaneous field of view (IFOV). This phenomenon is one of the most challenging sources of inaccuracy in the remote sensing study of land surfaces since the advent of high-resolution Earth observation satellites (Kiselev et al., 2015; Liang et al., 2001; Ouaidrari and Vermote, 1999; Pan et al., 2022; Reinersman and Carder, 1995; Sterckx et al., 2015). It depends on many factors: the spectral domain (Dave, 1980), the atmospheric conditions (Reinersman and Carder, 1995), the heterogeneity and anisotropic scattering of the target and its neighbouring land surfaces (Bulgarelli and Zibordi, 2018), and the light source and sensor configurations (Vermote et al., 1997), *etc*. In the study of (Bulgarelli and Zibordi, 2018) the adjacency effect reached 30% of the top of atmosphere (TOA) radiance signal at 443 nm at 1 km off the coast of northern Adriatic Sea and 15% at 5 km offshore. Therefore, neglecting it can lead to very inaccurate interpretations of remote sensing images.

Several methods to study and quantify the adjacency effect have been proposed since the late 1970's. They broadly belong to three groups: (1) empirical methods, (2) point spread function (PSF) based methods and (3) 3D radiative transfer (RT) modelling. Empirical methods (Minomura et al., 2001; Ouaidrari and Vermote, 1999; Richter, 1990) first derive individually the Lambertian reflectance $\rho^{(j)}$ of any pixel j from TOA reflectance assuming an infinite homogeneous plane ground, then approximate the adjacency effect on the TOA reflectance as the product of the averaged background reflectance $\langle\rho\rangle$ and the atmospheric diffuse

transmittance. $\langle\rho\rangle$ is the reflectance average over a $N \times N$ pixel window around the pixel of interest using the previously computed reflectance $\rho^{(j)}$. Being very fast, empirical methods are often used in operational atmospheric corrections (*e.g.*, Landsat TM). They use windows whose size N needs prior experience, mainly depending on the pixel size, the atmospheric condition, and the surface heterogeneity (Richter, 1990).

In PSF-based methods, the adjacency effect is defined by the atmospheric PSF $f(P, P_0, \Omega_i, \Omega_v)$ that gives the scattering contribution of a land surface point P illuminated in direction Ω_i to the observed point P_0 in direction Ω_v. The PSF can be computed analytically using the single scattering approximation (Kiselev et al., 2015; Santer and Schmechtig, 2000) or the two-stream approximation (Mekler and Kaufman, 1980). It can also be derived using a radiosity code (Borel and Gerstl, 1992) or using a Monte Carlo code (Adler-Golden et al., 2008; Miesch et al., 2005; Pearce, 1986; Reinersman and Carder, 1995). However, these methods tend to simplify the 3D RT mechanisms (*e.g.*, multiple scattering, 3D surface architecture, atmospheric RT) that give rise to the magnitude of the adjacency radiance.

A quantification of the adjacency radiance in remote sensing images needs a unified 3D RT modelling in a coupled Earth-Atmosphere system. This is increasingly possible as improvements in 3D RT modelling and computer technology reduce simulation times (Qi et al., 2019; Ramon et al., 2019; Wang et al., 2022). 3D RT modelling has recently been used to quantify the adjacency effect (Bulgarelli and Zibordi, 2018; Pan et al., 2022; Sun et al., 2021).

Most 3D RT models are either for the atmosphere and neglect the influence of the 3D structure and spatial heterogeneity of land surfaces (*e.g.*, 3DMCPOL, SPARTA) (Barlakas et al., 2016; Cornet et al., 2010) or for land surfaces and neglect the influence of the atmosphere (*e.g.*, librat,

raytran) (Govaerts et al., 1996; Lewis, 1999). Coupling a land surface RT model with an atmospheric RT model is often very approximate for simulating the adjacency effect, since it usually supposes a horizontal homogeneous land surface and atmospheric backscattering. This is why DART-FT (Flux-Tracking), the initial version of DART[1] (Gastellu-Etchegorry et al., 1996), included a radiative coupling mode, between the stratified atmosphere and the 3D land surface (Gascon et al., 2001; Grau and Gastellu-Etchegorry, 2013) instead of a coupling with an atmosphere model like MODTRAN (Berk and Hawes, 2017). DART-FT uses the discrete ordinates method (DOM) (Yin et al., 2013) to simulate the adjacency effect by convolving a pre-computed four-dimensional transfer function $\mathrm{TF}_{\mathrm{TOC}\to\mathrm{Z}}(\Delta i, \Delta j, \Omega, \Omega')$ that stores the incident power in direction Ω' at three image planes Z (any altitude, TOA, and top of canopy: TOC) with Δi line and Δj column shifts relative to point on the TOC plane that gives rise to a unit power in direction Ω. Pre-computing $\mathrm{TF}_{\mathrm{TOC}\to\mathrm{Z}}$ avoids repeated computations. However, it is only adapted to horizontally homogeneous atmosphere. Also, its efficiency greatly decreases with the increase in the numbers of atmospheric cells, and discrete directions Ω and Ω', whereas these numbers must be large to accurately simulate the adjacency effect, especially for high-resolution remote sensing images of spatially heterogeneous landscapes.

Since 2018, a Monte Carlo mode called DART-Lux has been implemented in DART to improve the accuracy and efficiency of simulations of TOC remote sensing images of large-and complex landscapes (Wang et al., 2022). Its end-to-end bidirectional path tracing algorithm samples a group of stochastic paths connecting the light source and the sensor and unbiasedly estimates radiance measurement using the weighted contribution of these path samples. DART-Lux

[1] DART (https://dart.omp.eu) is an ever-evolving radiative transfer model. It simulates the 3D radiative budget, including sun induced chlorophyll fluorescence, and remote sensing (RS) satellite, airborne and in-situ signals (spectroradiometer image, LiDAR FWF, SPL, point cloud) of natural and urban landscapes, from visible to thermal infrared. It is a reference tool for a wide range of RS studies (sensitivity studies, inversion of RS images, design of new RS sensor, etc.). Licenses are free for research and education.

results are consistent with those of DART-FT (relative difference < 1%) with simulation times and computer memory reduced by factors over 100 for complex landscapes (without atmosphere). Recently, (Wang and Gastellu-Etchegorry, 2021) designed a hybrid method that couples the Monte Carlo land surface RT and the DOM atmospheric RT to simulate satellite and airborne images. Although fast and accurate for relatively homogeneous land surfaces (*e.g.*, dense forest), this method is inefficient to simulate the adjacency effect, because its DOM atmospheric RT needs small atmospheric voxels. Although usually more efficient than Monte Carlo method for 1D surface-atmosphere coupling (*i.e.*, spatially constant TOC upwelling and downwelling fluxes), the DOM is much less efficient for 3D radiative coupling. Therefore, there was a need to design a Monte Carlo atmospheric RT modelling in DART, in addition to the DOM atmospheric RT.

This paper presents two improvements of DART-Lux to simulate remote sensing images with accurate account of atmospheric effects (*e.g.*, adjacency effect). 1) A new representation of the Earth-Atmosphere system. 2) A generalization of our initial formulation of RT modelling (Wang et al., 2022) to scenes with surfaces and volumes. In addition, the DART tool (*i.e.*, BRF camera) that simulates the scene TOC radiance at 1° x 1° angular resolution is adapted to any altitude level and angular resolution in order to quantify the adjacency effect on the scene radiance and albedo at TOA and TOC. Section 2 summarizes the Monte Carlo modelling of the initial version of DART-Lux for land surfaces. Section 3 presents the new representation of the Earth-Atmosphere system and the new formulation of atmospheric RT modelling. Section 4 presents the accuracy assessment of the new modelling and the study of the impact of the adjacency effect on TOA radiance and albedo. Finally, section 5 presents concluding remarks.

2 Principles of DART-Lux

DART-Lux is an unbiased Monte Carlo method for accurate and efficient simulation of remotely sensed images of large and complex landscapes (Wang et al., 2022). Its features useful for understanding the current work are summarized here. In DART-Lux, the 3D RT problem is described by a multi-dimensional integral and is solved with Monte Carlo integration methods. The radiance $L^{(j)}$ measured at a pixel j of the image is an integral over all the possible paths $\bar{r}$ from the light source to pixel j:

$$L^{(j)} = \int_{\mathcal{D}} f^{(j)}(\bar{r}) \cdot d\mu(\bar{r}) \quad (1)$$

with $\mathcal{D} = \bigcup_{n=1}^{\infty} \mathcal{D}_n$ the path space, $\mathcal{D}_n$ the set of paths $\bar{r}_n$ of length n, and $\bar{r}_n = r_0 r_1 ... r_n$ a series of vertices $r_{k=0...n}$ on surfaces $dA(r_k)$ of the scene with r_0 on the sensor and r_n on the light source. $\mu(\mathcal{D}_n) = \int_{\mathcal{D}_n} d\mu(\bar{r}_n) = \int_{\mathcal{D}_n} dA(r_n) \cdot dA(r_{n-1}) \cdots dA(r_0)$ is the area-product of $\mathcal{D}_n$. The term $f^{(j)}(\bar{r})$ represents the measurement contribution of a path $\bar{r}$. For a path $\bar{r}_n$:

$$f^{(j)}(\bar{r}_n) = L_e(r_n \to r_{n-1}) \cdot G(r_0 \leftrightarrow r_1) \cdot W_e^{(j)}(r_0 \to r_1) \prod_{k=2}^{n} f(r_k \to r_{k-1} \to r_{k-2}) \cdot G(r_{k-1} \leftrightarrow r_k) \quad (2)$$

with $f(r_k \to r_{k-1} \to r_{k-2})$ the bidirectional scattering distribution function (BSDF) at vertex r_{k-1}. It is often written as $f(r_k \leftrightarrow r_{k-1} \leftrightarrow r_{k-2})$ if there is Helmholtz reciprocity of scattering. L_e is the radiance emitted by the light source and W_e is the sensor importance function (*cf.* Appendix A in (Wang et al., 2022)) that transforms incident radiation into radiance. $G(r_{k-1} \leftrightarrow r_k) = V_t(r_{k-1} \leftrightarrow r_k) \cdot \frac{\cos\theta_i^{r_{k-1}} \cdot \cos\theta_o^{r_k}}{\|r_{k-1} - r_k\|^2}$ is a geometric term, with $V_t(r_{k-1} \leftrightarrow r_k)$ the visibility function: $V_t(r_{k-1} \leftrightarrow r_k)$ is 1 if r_{k-1} and r_k are mutually visible, and 0 otherwise. $\theta_i^{r_{k-1}}$ is the incident angle at vertex r_{k-1} and $\cos\theta_o^{r_k}$ is the exit angle at vertex r_k.

The importance sampling method, a major variance reduction technique in Monte Carlo integration (Rubinstein and Kroese, 2016), can unbiasedly estimate $L^{(j)}$ (Eq.) using:

$$F^{(j)} = \frac{f^{(j)}(\bar{r}_n)}{p(\bar{r}_n)} \quad (3)$$

with $F^{(j)}$ an estimate of $L^{(j)}$ and $p(\bar{r}_n)$ the probability of a path sample $\bar{r}_n$.

Eq. (3) indicates that $L^{(j)}$ can be efficiently derived if all paths $\bar{r}_n$ are fast sampled and the estimate $F^{(j)}$ converges with less repetitive scholastic processes. DART-Lux estimates $L^{(j)}$ with a robust and rapid bidirectional path tracing method. First, all vertices of two independent paths, one starting from the light source ($\bar{p}_N$=$p_0, p_1, ..., p_s, ..., p_{N\text{-}1}$) and one starting from the sensor ($\bar{q}_N$=$q_0, q_1, ..., q_t, ..., q_{N\text{-}1}$), are connected to get a group of random paths $\bar{r}_{s,t}$=$p_0, p_1, ..., p_{s\text{-}1}, q_{t\text{-}1}, q_{t\text{-}2}, ..., q_0$ (*cf.* Figure 5 in (Wang et al., 2022)). Then, the multiple importance sampling (MIS) estimator, proposed by (Veach and Guibas, 1997), computes $L^{(j)}$ using a weight $w_{s,t}(\bar{r}_{s,t})$ per path sample $\bar{r}_{s,t}$ (Eq. (4)). In general, a larger weight corresponds to a path sample with large probability density function (Wang et al., 2022).

$$F_{\mathrm{MIS}}^{(j)} = \sum_{s\geq 0}\sum_{t\geq 0} w_{s,t}(\bar{r}_{s,t}) \cdot \frac{f^{(j)}(\bar{r}_{s,t})}{p(\bar{r}_{s,t})} \quad (4)$$

3 Atmospheric radiative transfer modelling

The initial version of DART-Lux (Wang et al., 2022) simulated RT with a Monte Carlo method for Earth scenes (*i.e.*, landscapes) represented by surfaces (*i.e.*, facets), and with the DOM mode of DART-FT for the atmosphere. As it was not suitable for simulating the adjacency effect, we designed a new representation of the Earth-Atmosphere system and generalized the theorical formulation of DART-Lux to Earth scenes that contain both surfaces and volumes.

3.1 New Earth-Atmosphere system

The new Earth-Atmosphere scene (Figure 1) is a square cuboid that contains the atmosphere and a region of interest (ROI) at its bottom centre, surrounded by a horizontal background with

user-defined bi-directional reflectance (*e.g.*, Lambertian, Rahman-Pinty-Verstraete (RPV), specular). The ROI is a 3D landscape that includes the observed target. Its topography is smoothly connected to the background by the Bézier triangle (Farin, 2014; Wang et al., 2020). The optical properties of foliar and soil surfaces can be defined using the DART database of optical properties, or computed by the PROSPECT / Fluspect / MARMIT modules (Bablet et al., 2018; Dupiau et al., 2022; Féret et al., 2017; Jacquemoud and Baret, 1990; Vilfan et al., 2016). The atmosphere (*i.e.*, gases and, aerosols) is made of horizontally homogeneous and vertically continuous layers with any depths, at any altitudes; default depths are 1 km from 0 to 15 km altitude and 5 km from 15 to 50 km altitude. Polynomials from the spline interpolation ensure vertical continuity of optical properties (*e.g.*, extinction coefficient) and temperature within and between layers (Wang and Gastellu-Etchegorry, 2020). Clouds can be imported as 3D volumes with defined shape and homogenous properties. The scene default size is 500 km × 500 km× 50 km, which is a good approximation of infinite plane-parallel atmosphere with relative difference less than 0.1% (*cf.* Appendix A). The DART atmosphere database includes six standard gas models (*i.e.*, TROPICAL, MIDLATSUM, MIDLATWIN, SUBARCSUM, SUBARCWIN and USSTD76 (Anderson et al., 1986)) and five standard aerosol models (*i.e.*, Rural, Urban, Maritime, Tropospheric and Fog (Shettle and Fenn, 1979)). These models can be adapted and data (*e.g.*, gas and temperature profiles) can be imported to match actual atmospheric conditions. The methods to compute the atmospheric vertical profiles are detailed in (Wang and Gastellu-Etchegorry, 2020). In this new Earth-Atmosphere scene, the sensor can be anywhere with any orientation and field of view (FOV).

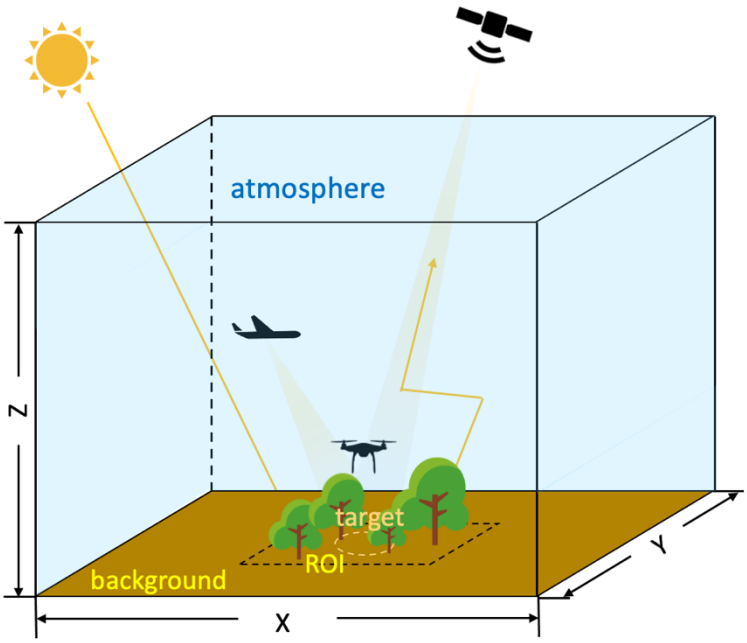

Figure 1. The DART-Lux Earth-Atmosphere system: square cuboid filled by the atmosphere and a 3D landscape (region of interest: ROI) at its bottom centre, surrounded by a horizontal background. The observed target is in the ROI. Default size: X × Y × Z = 500 km × 500 km × 50 km.

The DART BRF camera gives the TOC radiance of the total scene at 1° x 1° angular resolution (Wang et al., 2022). It was adapted in order to give the directional radiance at any altitude from the ground to TOA, for any user-defined angular resolution and scene sub-zones. It provides the directional radiance measured from a user-defined virtual surface Σ. Figure 2 shows its three modes. In mode 1, the BRF camera provides the average directional radiance of Σ measured at Σ. In mode 2, it provides the average directional radiance at a given distance to the centre of Σ. In mode 3, it provides the average directional radiance of Σ measured at a given altitude.

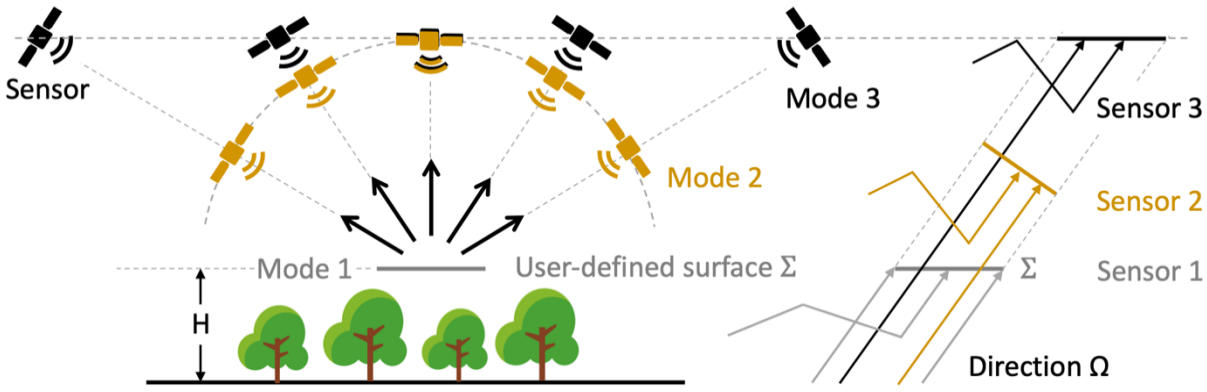

Figure 2. The three modes of the improved BRF camera. They give the radiance from a user-defined surface Σ at altitude H, for any angular resolution and range. Mode 1: average directional radiance measured at Σ. Mode 2: average directional radiance measured at a given distance to the centre of Σ. Mode 3: average directional radiance measured at any user-defined altitude.

3.2 Light transport equation

3.2.1 Radiative transfer equation and its formal solution

Eq. (1) is not adapted to simulate the propagation of radiation in fluids (*e.g.*, atmosphere) and vegetation volumes treated as turbid media. Then, an integro-differential equation gives the change of radiance per unit distance $\frac{dL}{ds}$ in the considered ;medium at location r in direction Ω. For fluids, this equation is:

$$\frac{dL(r,\Omega)}{ds} = -\alpha_t(r)\cdot L(r,\Omega) + \frac{\alpha_s(r)}{4\pi}\cdot\int_{4\pi} L(r,\Omega')\cdot P(r,\Omega'\rightarrow\Omega)d\Omega' + \frac{dL_e(r,\Omega)}{ds} \qquad (5)$$

with α_t the extinction coefficient and α_s the scattering extinction coefficient. α_t is assumed invariant to rotation: $\alpha_t(r,\Omega)=\alpha_t(r)$, as in a medium filled with microscopically isotropic and mirror-symmetric particles (Mishchenko et al., 2006). The unit normalized scattering phase function $P(r,\Omega'\rightarrow\Omega)$ ($\frac{1}{4\pi}\int_{4\pi} P(r,\Omega'\rightarrow\Omega)d\Omega=1$) gives the angular distribution of the scattered power to direction Ω due to the incident power from direction Ω'. The term $\frac{dL_e}{ds}$ is the variation of thermal radiance, *i.e.*, the Planck function, per unit distance. The notation of

incident direction Ω' differs for volume and surface scattering: it usually points towards the interaction location in volume scattering and usually points away from the interaction location in surface scattering.

Because it is an integro-differential equation, Eq. (5) is transformed to an integral form (Eq. (6)) that a Monte Carlo algorithm can solve. Eq. (6) shows that radiance $L(r,\Omega)$ at a point r in a medium is the sum of (1) radiance $L(r_0,\Omega)$ at r_0 transmitted to r, and (2) cumulated scattering and thermal emission from r_0 to r (Figure 3).

$$L(r,\Omega)=L(r_0,\Omega)\cdot\mathcal{T}(r\leftrightarrow r_0)+\int_0^s[\frac{\alpha_s(r')}{4\pi}\int_{4\pi}L(r',\Omega')\cdot P(r',\Omega'\rightarrow\Omega)\cdot d\Omega'+\frac{\partial L_e(r',\Omega)}{\partial s'}]\cdot\mathcal{T}(r\leftrightarrow r')\cdot ds' \quad (6)$$

with $s=\|r-r_0\|$ the distance between r and r_0, $r'=r-s'\Omega$ the location at the distance s' from r in direction Ω, and $\mathcal{T}(r\leftrightarrow r_0)=\exp\left(-\int_0^s\alpha_t(r')ds'\right)$ the transmittance from r_0 to r. The left-right arrow emphasizes the Helmholtz reciprocity principle (i.e., $\mathcal{T}(r_0\rightarrow r)=\mathcal{T}(r\rightarrow r_0)$).

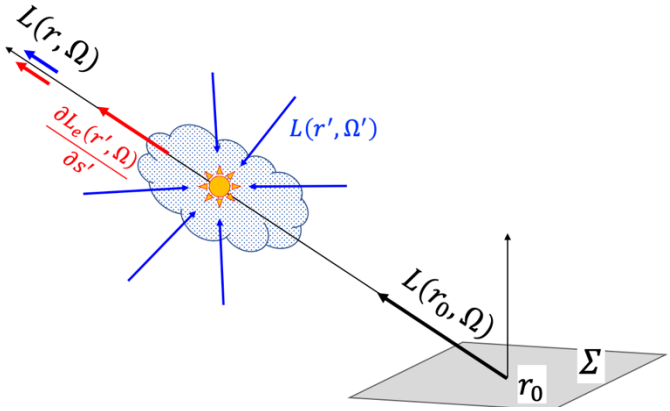

Figure 3. Radiance $L(r,\Omega)$ at r. It is the sum of radiance $L(r_0,\Omega)$ at r_0 of a surface Σ that is transmitted to r, and radiance due to scattering and thermal emission along the path $\overrightarrow{r_0r}$.

3.2.2 Unified light transport equation for the surface and the volume

In an infinite medium, Eq. (6) becomes $L(r,\Omega)=\int_0^\infty\frac{\partial L(r',\Omega)}{\partial s'}\cdot\mathcal{T}(r\leftrightarrow r')\cdot ds'$ with:

$$\frac{\partial L(r',\Omega)}{\partial s'}=\int_{4\pi}L\left(r',\Omega'\right)\cdot\frac{\alpha_s(r')\cdot P(r',\Omega'\rightarrow\Omega)}{4\pi}\cdot d\Omega'+\frac{\partial L_e(r',\Omega)}{\partial s'} \quad (7)$$

Eq. (7) becomes an integral over volume V by replacing directions with pairs of vertices (*e.g.*, $\Omega \equiv (r' \rightarrow r)$), and solid angle $d\Omega'$ by $\frac{dA(r'')}{\|r''-r'\|^2}$, and using the visibility function $V_t(r'' \leftrightarrow r')$:

$$\frac{\partial L(r' \rightarrow r)}{\partial s'} = \int_V \frac{\partial L(r'' \rightarrow r')}{\partial s''} \cdot \frac{\alpha_s(r') \cdot P(r'' \rightarrow r' \rightarrow r)}{4\pi} \cdot \frac{V_t(r'' \leftrightarrow r') \cdot \mathcal{T}(r'' \leftrightarrow r')}{\|r'' - r'\|^2} \cdot dV(r'') + \frac{\partial L_e(r' \rightarrow r)}{\partial s'} \quad (8)$$

Since the derived volume light transport equation (Eq. (8)) and the surface light transport equation (Wang et al., 2022) have a similar formulation, a unified formulation can be used:

$$\tilde{L}(r' \rightarrow r) = \tilde{L}_e(r' \rightarrow r) + \int_{\mathcal{M}} \tilde{L}(r'' \rightarrow r') \cdot \tilde{f}_s(r'' \rightarrow r' \rightarrow r) \cdot \tilde{G}(r' \leftrightarrow r'') \cdot d\mathcal{M}(r'') \quad (9)$$

with $\mathcal{M}$ a surface A or volume V depending on the material at the vertex. The radiance terms $\tilde{L}$ and $\tilde{L}_e$ correspond to radiance for a surface, and radiance per unit distance for a volume:

$$\tilde{L}(r'' \rightarrow r') = \begin{cases} L(r'' \rightarrow r') & \forall\, r' \in A \\ \dfrac{\partial L(r'' \rightarrow r')}{\partial s''} & \forall r' \in V \end{cases}$$

The scattering distribution function $\tilde{f}$ is either the BSDF for a surface, or the product of the scattering extinction coefficient and the scattering phase function for a volume:

$$\tilde{f}_s(r'' \rightarrow r' \rightarrow r) = \begin{cases} f_s(r'' \rightarrow r' \rightarrow r) & \forall\, r' \in A \\ \alpha_s(r') \cdot \dfrac{P(r'' \rightarrow r' \rightarrow r)}{4\pi} & \forall\, r' \in V \end{cases}$$

The generalized geometric term $\tilde{G}(r' \leftrightarrow r'') = V(r' \leftrightarrow r'') \cdot \mathcal{T}(r'' \leftrightarrow r') \cdot \frac{\tilde{\mu}_o^{r'} \cdot \tilde{\mu}_i^{r''}}{\|r''-r'\|^2}$ is defined with:

$$\tilde{\mu}_o^{r'} = \begin{cases} \cos\theta_o^{r'} & \forall\, r' \in A \\ 1, & \forall\, r' \in V \end{cases} \text{ and } \tilde{\mu}_i^{r''} = \begin{cases} \cos\theta_i^{r''} & \forall\, r'' \in A \\ 1, & \forall\, r'' \in V \end{cases}$$

3.2.3 Path integral formulation

In an interaction, the incident radiance is the path attenuated exit radiance from a previous interaction. Therefore, Eq. (9) is iteratively expanded to an infinite sum of multidimensional integrals where each integral is the contribution of a specific scattering order to $\tilde{L}(r_1 \rightarrow r_0)$:

$$\tilde{L}(r_1 \rightarrow r_0) = \tilde{L}_e(r_1 \rightarrow r_0) + \int_{\mathcal{M}} \tilde{L}_e(r_2 \rightarrow r_1) \cdot \tilde{f}_s(r_2 \rightarrow r_1 \rightarrow r_0) \cdot \tilde{G}(r_1 \leftrightarrow r_2) \cdot d\mathcal{M}(r_2)$$

$$+\int_{\mathcal{M}}\int_{\mathcal{M}}\tilde{L}_e(r_3\to r_2)\cdot\tilde{f}_s(r_3\to r_2\to r_1)\cdot\tilde{G}(r_2\leftrightarrow r_3)\cdot\tilde{f}_s(r_2\to r_1\to r_0)\cdot\tilde{G}(r_1\leftrightarrow r_2)\cdot d\mathcal{M}(r_3)\cdot d\mathcal{M}(r_2)+\ldots$$

Since $r_1\to r_0$ is the direction to the sensor, the radiance measurement $L^{(j)}$ at pixel j is computed by integrating $\tilde{L}(r_1\to r_0)$ weighted by the importance function $W_e{}^{(j)}(r_0\to r_1)$ of the sensor:

$$\tilde{L}^{(j)}=\int_A\int_{\mathcal{M}}W_e{}^{(j)}(r_0\to r_1)\cdot\tilde{L}(r_1\to r_0)\cdot\tilde{G}(r_0\leftrightarrow r_1)\cdot d\mathcal{M}(r_1)\cdot dA(r_0) \tag{10}$$

$L^{(j)}$ is a Lebesgue integral over the space $\tilde{\mu}$ of surfaces and volumes of the set of paths $\widetilde{\mathcal{D}}$:

$$\tilde{L}^{(j)}=\int_{\widetilde{\mathcal{D}}}\tilde{f}^{(j)}(\bar{r})\cdot d\tilde{\mu}(\bar{r}) \tag{11}$$

$\widetilde{\mathcal{D}}_n$ and $\tilde{\mu}(\widetilde{\mathcal{D}}_n)$ are generalized paths that intersect surfaces and volumes, with $\widetilde{\mathcal{D}}_n$ the multiple cartesian product of the space $\{A,V\}$, since a vertex is either in a volume V or on a surface A.

$$\widetilde{\mathcal{D}}_n=\bigcup_{c\in\{0,1\}^n}(A\times\mathcal{M}_1\times\cdots\times\mathcal{M}_n),\text{ with }\mathcal{M}_k=\begin{cases}A, c_k=0\\ V, c_k=1\end{cases}$$

$$\tilde{\mu}(\widetilde{\mathcal{D}}_n)=\int_{\mathcal{D}_n}d\mu(\bar{r}_n)=\sum_{c\in\{0,1\}^n}\int_{(A\times\mathcal{M}_1\times\cdots\times\mathcal{M}_n)}dA(r_0)\cdot\prod_{k=1}^{n}\begin{cases}dA(r_k), & c_k=0\\ dV(r_k), & c_k=1\end{cases}$$

with Cartesian product such that $\{0,\ 1\}^n=\left\{(c_1,c_2,\cdots,c_k,\cdots,c_n)\,|\,c_k\in\{0,\ 1\}\ \forall\, k\in\{1,2,\cdots,n\}\right\}$.

For example, $\widetilde{\mathcal{D}}_1=(A\times A)+(A\times V)$ describes a surface emission and a volume emission event. $\widetilde{\mathcal{D}}_2=(A\times A\times A)+(A\times A\times V)+(A\times V\times A)+(A\times V\times V)$ describes a surface emission followed by a surface scatter event, a surface emission followed by a volume scatter event, a volume emission followed by a surface scatter event and a volume emission followed by a volume scatter event, and so on. Therefore, integration over $\widetilde{\mathcal{D}}_n$ is the sum of 2^n (n+1)-dimensional integrals.

The unified contribution function $f^{(j)}(\bar{r}_n)$ uses the unified quantities for both surfaces and volumes in the formulation in Eq. (2):

$$\tilde{f}^{(j)}(\bar{r}_n)=\tilde{L}_e(r_n\to r_{n-1})\cdot\tilde{G}(r_0\leftrightarrow r_1)\cdot W_e{}^{(j)}(r_1\to r_0)\cdot\prod_{k=2}^{n}\tilde{f}_s(r_k\to r_{k-1}\to r_{k-2})\cdot\tilde{G}(r_{k-1}\leftrightarrow r_k) \quad (12)$$

Thus, a unified algorithm handles surface and volume interactions. Differences are only in assessing the effective source emission, scattering distribution function, and geometric term at each vertex r_k according to the material. (Regaieg, 2023) describes its adaptation to vegetation treated as turbid medium.

3.3 Radiative transfer modelling

As the Earth-Atmosphere system (Figure 1) has a huge size (*i.e.*, X × Y × Z = 500 km × 500 km × 50 km) compared to ROI, the forward random walk from the light source is inefficient. For example, a ray from a source located 200 km away from the ROI has a very small probability to be scattered into the sensor FOV. In addition, its intersection with a scene element (*e.g.*, a leaf) can be very inaccurate due to computer decimal imprecision. Therefore, because it is time consuming and inaccurate, the forward random walk is deactivated for simulating Monte Carlo surface-atmosphere RT. In short, a random virtual ray is emitted from the sensor, and is connected to the light source after each interaction with a volume or a surface, using a user defined maximal scattering order M to limit the path length. Then, the estimator in Eq. (4) is:

$$F_{\mathrm{IS}}^{(j)}=\sum_{n=1}^{\infty}\frac{\tilde{f}^{(j)}(\bar{r}_n)}{p(\bar{r}_n)} \quad (13)$$

3.3.1 Light scattering

The sampling of a stochastic path $\bar{r}_n$ and the evaluation of the path contribution $\frac{\tilde{f}^{(j)}(\bar{r}_n)}{p(\bar{r}_n)}$ are detailed here. The scattering direction is sampled with the angular distribution of the exit power due to unit incident power. For surfaces, the probability density function (PDF) for incident direction -Ω_i (minus sign as Ω_i is defined from the scattering point) and exit direction Ω_o is:

$$p(\Omega_o|\text{-}\Omega_i) = \begin{cases} P^* \cdot \dfrac{\tilde{f}(r, \text{-}\Omega_i \to \Omega_o) \cdot \cos\theta_o}{\int_{2\pi} \tilde{f}\left(r, \text{-}\Omega_i \to \Omega_o^{'}\right) \cdot \cos\theta_o^{'} \, d\Omega_o^{'}}, & \text{if } (\vec{n} \cdot \Omega_o) \cdot (\vec{n} \cdot \Omega_i) \geq 0 \\ (1 - P^*) \cdot \dfrac{\tilde{f}(r, \text{-}\Omega_i \to \Omega_o) \cdot \cos\theta_o}{\int_{2\pi} \tilde{f}\left(r, \text{-}\Omega_i \to \Omega_o^{'}\right) \cdot \cos\theta_o^{'} \, d\Omega_o^{'}}, & \text{otherwise} \end{cases} \quad (14)$$

with P^* the reflection probability and $\vec{n}$ the surface normal. $p(\Omega_i|\text{-}\Omega_o)$ is similarly defined.

The conditional PDF of volume scattering (isotropic mirror-symmetric microscopic particles) is:

$$p(\Omega_o|\Omega_i) = \frac{\tilde{f}(r, \Omega_i \to \Omega_o)}{\int_{4\pi} \tilde{f}\left(r, \Omega_i \to \Omega_o^{'}\right) d\Omega_o^{'}} = \frac{P(r, \Omega_i \to \Omega_o)}{4\pi} \quad (15)$$

with $p(\Omega_i|\Omega_o)$ being similarly defined.

Two types of atmospheric scattering implemented in DART are presented here:

- ***Rayleigh scattering*** (particles with diameter d such that $0.002 < \frac{\pi d}{\lambda} < 0.2$) (Petty, 2006)

The Rayleigh phase function uses the phase angle γ ($\cos\gamma = |\Omega_i \cdot \Omega_o|$) and a depolarization factor δ to consider the influence of molecule anisotropy. δ is a spectral quantity (Bates, 1984; Bucholtz, 1995) that decreases from 0.04545 at 0.2 μm down to 0.02955 at 0.4 μm, 0.02730 at 0.8 μm, and is nearly constant for longer wavelengths. Its relative influence on Rayleigh scattering phase function of dry air is smaller than 0.1% for wavelengths larger than 0.4 μm. It is commonly assumed to be equal to 0.0279, as advised by (Young, 1980):

$$P(r, \Omega_i \to \Omega_o) = \frac{3}{2} \cdot \frac{1 - \delta}{2 + \delta} \cdot \left(\frac{1 + \delta}{1 - \delta} + \cos^2\gamma\right) \quad (16)$$

- ***Particle scattering*** (particles with diameter d such that $\frac{\pi d}{\lambda} > 0.2$)

The double Henyey-Greenstein phase function simulates it, with asymmetry factors $g_1 > 0$ (forward scattering) and $g_2 < 0$ (backward scattering) and ratio a of forward scattering:

$$P(r, \Omega_i \to \Omega_o) = \frac{a \cdot (1 - {g_1}^2)}{(1 + {g_1}^2 - 2g_1 \cdot \cos\gamma)^{3/2}} + \frac{(1 - a) \cdot (1 - {g_2}^2)}{(1 + {g_2}^2 - 2g_2 \cdot \cos\gamma)^{3/2}} \quad (17)$$

3.3.2 Light transmission

Once an exit direction Ω_o is sampled at r, an intersection test along Ω_o gives the intersected vertex on the nearest surface (Figure 4). If there is no medium in the line of sight, the process continues by sampling the next scattering direction at the intercepted vertex. Otherwise, a free path S in the medium is sampled according to the path PDF $p(s)$ and the cumulative distribution function $P_S(s)$ (*i.e.*, $\mathbb{P}(S \leq s)$):

$$P_S(s) = \mathbb{P}(S \leq s) = 1 - \mathcal{T}(s) \quad \text{and} \quad p(s) = \frac{dP_S(s)}{ds} = \alpha_t(s) \cdot \mathcal{T}(s) \tag{18}$$

with $\mathcal{T}(s)$ the transmittance from r to $r + s{\cdot}\Omega_o$ along Ω_o and $\alpha_t(s)$ the extinction coefficient at $r + s{\cdot}\Omega_o$. If the signal is modelled for a series of spectral bands, α_t is an average extinction coefficient for all spectral bands.

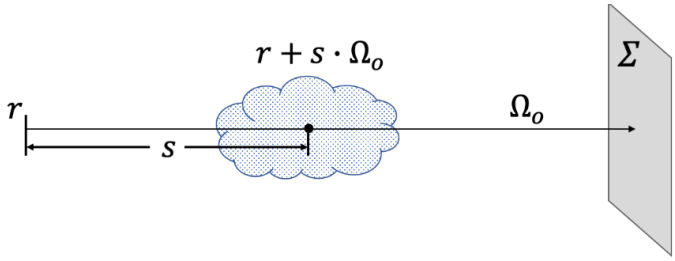

Figure 4. Distance sampling schema. s is the distance from the start location r to the current location $r{+}s{\cdot}\Omega_o$ in direction Ω_o. Σ is the nearest surface in the direction of propagation.

The probabilistic free path S is derived from a random variable $\xi \in [0, 1)$ and an inversion function $S = P_S^{-1}(\xi)$. For a homogeneous medium (*i.e.*, constant α_t in the line of sight):

$$S = P_S^{-1}(\xi) = -\frac{\ln(1 - \xi)}{\alpha_t} \tag{19}$$

Usually, α_t varies in the line of sight, and S cannot be derived analytically. Then, the medium is represented by discrete volumes and the free path is sampled with the *Regular Tracking* method (Amanatides and Woo, 1987). For example, for a series of homogeneous segment medium along the line of sight, each one with extinction coefficient α_i and segment length Δs_i:

$$p(s) = \alpha_i \cdot e^{-[\sum_{k=0}^{i-1} \alpha_k \cdot \Delta s_k + \alpha_i \cdot (s - \sum_{k=0}^{i-1} \Delta s_k)]}$$

$$P_S(s) = 1 - e^{-[\sum_{k=0}^{i-1} \alpha_k \cdot \Delta s_k + \alpha_i \cdot (s - \sum_{k=0}^{i-1} \Delta s_k)]} \qquad \forall\, s \in [\sum_{k=0}^{i-1} \Delta s_k\,,\, \sum_{k=0}^{i} \Delta s_k] \tag{20}$$

The free path equation $S = P_S^{-1}(\xi)$ is solved recursively until the path optical depth gives the randomly sampled value $-\ln(1 - \xi)$:

$$-\ln(1 - \xi) = \sum_{k=0}^{i-1} \alpha_k \cdot \Delta s_k + \alpha_i \cdot \left(S - \sum_{k=0}^{i-1} \Delta s_k\right)$$

Once sampled, if the free path S is less than the distance s_Σ to the nearest surface (Figure 4), it defines the next scattering event in the medium. If $S \geq s_\Sigma$, the sampled vertex is on the nearest surface and the path probability density is multiplied by the probability $\mathbb{P}(S \geq s_\Sigma) = \int_{s_\Sigma}^{\infty} p(s)ds = \mathcal{T}(s_\Sigma)$ that the ray will be intercepted by the nearest surface.

3.3.3 Measurement evaluation

Starting from the sensor, a complete path is created by repeatedly sampling a vertex and free path. In detail, a vertex r_0 on the lens and an emitted virtual ray direction Ω_0 are first sampled using sensor characteristics. Then, a vertex r_k is created by sampling a stochastic exit direction $\Omega_{k\text{-}1}$ at the vertex $r_{k\text{-}1}$. This sampling depends only on the local incident direction $r_{k\text{-}2} \rightarrow r_{k\text{-}1}$. The free path is always sampled after each bounce. Finally, the last vertex r_n on the light source is generated by uniformly sampling the solid angle subtended by the light source at the previous vertex $r_{n\text{-}1}$. Here the free path is not sampled. Instead, we force the radiation to connect the light source to increase the efficiency. The path PDF is evaluated by:

$$p(\bar{r}_n) = p(r_0) \cdot p(r_1|r_0) \cdot \prod_{k=2}^{n-1} p(r_k|r_{k-1}, r_{k-2}) \cdot p(r_n|r_{n-1}) = \prod_{k=0}^{n} \overleftarrow{p}(r_k) \tag{21}$$

Eq. (22) shows the expression of PDF $p(r_k|r_{k\text{-}1}, r_{k\text{-}2}, \ldots, r_0) \equiv \overleftarrow{p}(r_k)$ for $1 < k < n$ with a reverse arrow to indicate that it is for backward light transport (*cf.* Appendix C in (Wang et al., 2022)). PDFs $p(r_0) \equiv \overleftarrow{p}(r_0)$, $p(r_1|r_0) \equiv \overleftarrow{p}(r_1)$ and $p(r_n|r_{n\text{-}1}) \equiv \overleftarrow{p}(r_n)$ can be derived in a similar way.

$$\overleftarrow{p}(r_k) = \begin{cases} p(\Omega_{k-1}) \cdot \dfrac{\mathcal{T}(r_{k-1} \leftrightarrow r_k) \cdot \cos\theta_o^{r_k}}{\|r_{k-1} - r_k\|^2} & \forall r_k \in A \\ p(\Omega_{k-1}) \cdot \dfrac{\alpha_e(r_k) \cdot \mathcal{T}(r_{k-1} \leftrightarrow r_k)}{\|r_{k-1} - r_k\|^2} & \forall r_k \in V \end{cases} \quad (22)$$

The contribution function $\tilde{f}^{(j)}(\bar{r}_n)$ is computed as in Eq. (12):

$$F_{\mathrm{IS}}^{(j)} = \sum_{n=1}^{\infty} \frac{\tilde{L}_e(r_n \to r_{n\text{-}1}) \cdot \tilde{G}(r_0 \leftrightarrow r_1) \cdot W_e^{(j)}(r_0 \to r_1)}{\overleftarrow{p}(r_0) \cdot \overleftarrow{p}(r_1)} \cdot \prod_{k=2}^{n} \frac{\tilde{f}(r_k \leftrightarrow r_{k\text{-}1} \leftrightarrow r_{k\text{-}2}) \cdot \tilde{G}(r_{k\text{-}1} \leftrightarrow r_k)}{\overleftarrow{p}(r_k)} \quad (23)$$

Eq. (23) is analysed in Appendix B for a semi-infinite plane parallel atmosphere, illuminated by parallel sunlight and observed by a TOA orthographic camera. Results are consistent with the familiar Single Scattering Albedo (SSA) method (Spada et al., 2006).

4 Model assessment and application

DART-Lux already proved to be accurate (Wang et al., 2022) for land surfaces, as compared with Monte Carlo models in the RAMI experiment (Widlowski et al., 2007), and remote sensing and in-situ measurements (Malenovsky et al., 2023, Liu et al., 2023). For example, (Landier et al., 2018) noted a urban TOC albedo (ratio of upward exitance and downward irradiance) relative difference ≈ 2.5% between in-situ measurements and simulations using satellite-derived optical properties of urban elements. This section presents the assessment of DART accuracy for the adjacency effect modelling, including a quantitative study on this effect.

4.1 Accuracy assessment

DART accuracy in atmospheric RT modelling, in particular the adjacency effect, was assessed with the Monte Carlo atmospheric model SMART-G (Ramon et al., 2019), already validated with the reference MYSTIC model in the International Polarized Radiative Transfer (IPRT) intercomparison study (https://www.meteo.physik.uni-muenchen.de/~iprt/doku.php). SMART-G is developed by HYGEOS (https://www.hygeos.com) for the French space agency (CNES)

to simulate light propagation in the atmosphere and oceans. Our assessment consists of two phases using atmospheric parameters of case B2 (https://www.meteo.physik.uni-muenchen.de/~iprt/doku.php?id=intercomparisons:b2_absorption) of the IPRT study (Emde et al., 2015). This atmosphere has 30 equal-thickness (1 km) layers, with given absorption and scattering optical thickness per layer. Table 1 shows the DART and SMART-G configurations.

Table 1. Simulation configurations for Phase 1 and Phase 2 comparisons.

	Phase 1	**Phase 2**
Atmosphere model	IPRT case B2	IPRT case B2
Land surface	Infinite black surface	Black disc (R = 2 km) + Infinite white environment
Solar direction	SZA = 60° SAA = 0°	SZA = 0° and 30° SAA = 270°
Sensor altitude	30 km (TOA)	30 km (TOA)
Output	Directional reflectance for: VZA 0° – 80° with 5° step VAA 0° – 180° with 5° step	Nadir image of the disc: Spatial resolution: 10 m Image size: 400 × 400

In phase 1, DART and SMART-G agree (Figure 5): the relative root mean square difference $\varepsilon_{\text{DART}}^{\text{SMART-G}} = 0.20\%$ for 629 upward viewing directions (Table 1), by considering $\varepsilon_{\text{model}}^{\text{reference}} = \frac{\sqrt{\sum_{i=1}^{N}\left(\rho_{\text{model}}(i)-\rho_{\text{reference}}(i)\right)^2}}{\sqrt{\sum_{i=1}^{N}\rho_{\text{reference}}(i)^2}}$ (Emde et al., 2015). This small value is mainly due to Monte Carlo noise and rounding errors in calculations. The squared-average TOA reflectance $\sqrt{\frac{\sum_{i=1}^{N}\left(\rho_{\text{SMART-G}}(i)\right)^2}{N}}$ is 0.04866, with maximum standard deviation $\sigma_{\text{Max}}^{\text{SMART-G}} = 1.1\times10^{-5}$ and $\sigma_{\text{Max}}^{\text{DART}} = 3.8\times10^{-5}$. It gives composed standard deviation $\sigma_{\text{Max}}^{\text{tot}} = \sqrt{(\sigma_{\text{Max}}^{\text{SMART-G}})^2+\left(\sigma_{\text{Max}}^{\text{DART}}\right)^2} = 4.0\times10^{-5}$ and maximum tolerated relative difference $\frac{3\times\sigma_{\text{tot}}}{0.04866} = 0.25\%$, which is a probability of 99.7% the

relative difference $\varepsilon_{DART}^{SMART\text{-}G}$ lies in 0.25%. Compared to the proposed reference model MYSTIC in IPRT program, the relative differences are $\varepsilon_{DART}^{MYSTIC} = 0.21\%$ and $\varepsilon_{SMART\text{-}G}^{MYSTIC} = 0.013\%$.

In phase 2, we determined the horizontal profiles of average TOA reflectance of the black disc[2] from its centre to its edge, with a step of 0.1 km, for two solar directions[3] (SZA = 0° and SZA = 30°) (Figure 6). The adjacency effect clearly increases from the centre to the edge of the disc. The relative root mean square difference is 0.033% for SZA = 0° and 0.032% for SZA = 30°. These small differences are due to Monte Carlo noise and rounding error in calculations. Indeed, the average TOA nadir reflectance of the disc is 0.137 for SZA = 0° and 0.114 for SZA = 30°, while DART and SMART-G maximum standard deviations are $\sigma_{MAX}^{SMART\text{-}G} = 6 \times 10^{-6}$ and $\sigma_{MAX}^{DART} = 1.8 \times 10^{-5}$. Then, composed standard deviation $\sigma_{MAX}^{tot} = \sqrt{\left(\sigma_{MAX}^{SMART-G}\right)^2 + (\sigma_{MAX}^{DART})^2} = 1.9 \times 10^{-5}$ and maximum tolerated relative difference $\frac{3 \times \sigma_{tot}}{0.114} = 0.05\%$.

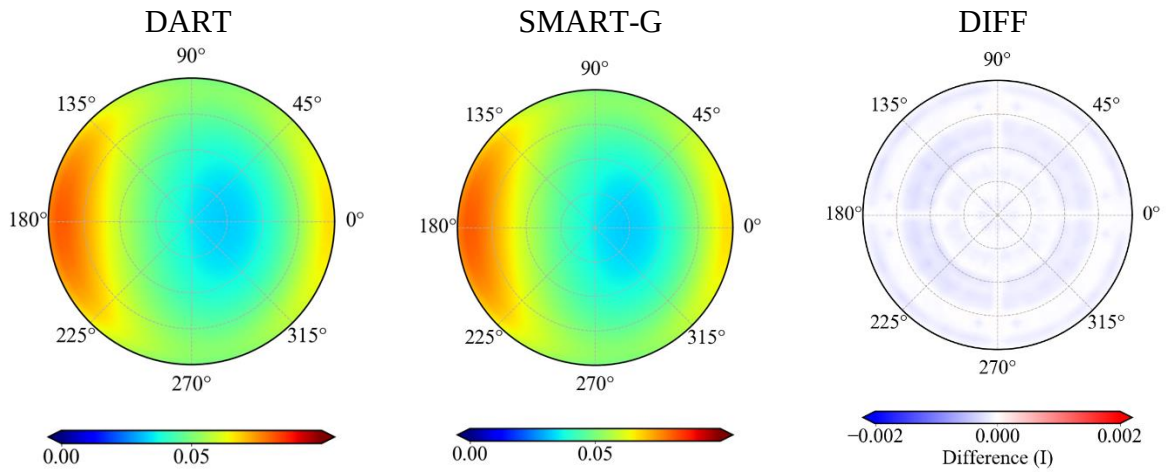

Figure 5. DART and SMART-G TOA directional reflectance and difference in phase 1, from left to right. Simulation parameters are indicated in Table 1.

[2] In phase 2, DART simulates a nadir 400 x 400 image with spatial resolution of 10 m while SMART-G simulates 1.6 x 10^5 sensors that are positioned at each pixel center of the image.

[3] The solar direction in DART is defined as a vector in local coordinates pointing towards the sun. Azimuth is measured from the north-south axis in an anticlockwise manner.

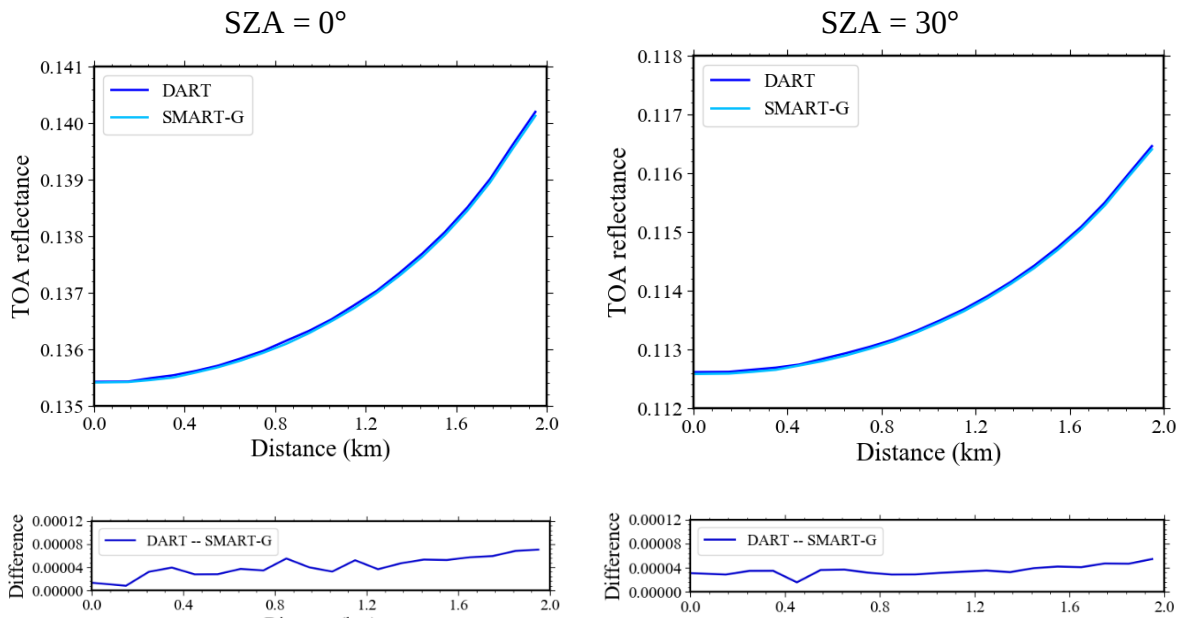

Figure 6. DART and SMART-G TOA reflectance value and difference from centre to edge of black disc for sun zenith angle (SZA) = 0° and 30°. Simulation parameters are in Table 1.

4.2 3D modelling of the adjacency effect

4.2.1 The experiment

The influence of the adjacency effect on target radiance and albedo is shown for four Sentinel-2A bands: blue (B: λ=0.4924 μm, $\Delta\lambda$=0.066 μm), green (G: λ=0.5598 μm, $\Delta\lambda$=0.036 μm, red (R: λ=0.6646 μm, $\Delta\lambda$=0.031 μm) and near infrared (NIR: λ=0.8328 μm, $\Delta\lambda$=0.106 μm). The atmosphere is defined by the USSTD76 gas model, and the Rural aerosol model. Table 2 gives its vertical scattering and absorption optical depth per band. Solar zenith and azimuth angles are θ_s=30° and φ_s=270°, respectively. The target is a circular city with a 2 km radius in a 3D neighbourhood of 10 km sides inside a 500 km square Lambertian plane background (Figure 7). The city has 55828 houses in regular rows (tiled roofs, concrete wall) and streets (asphalt roads), with optical properties of urban materials (*e.g.*, asphalt, concrete, tile) from the

SLUM (http://www.met.reading.ac.uk/micromet/LUMA/SLUM.html) and ECOSTRESS (https://speclib.jpl.nasa.gov) libraries. Two cases are considered (Figure 8):

- 3D case (Figure 8): the neighbourhood is a 10 km × 10 km 3D forest with 1553504 nearly-randomly located Tilia cordata trees at five growing stages, with homogeneous understory. The tree models and optical properties, including those of the understory, are from the RAMI experiment (https://rami-benchmark.jrc.ec.europa.eu/_www/index.php).
- 1D case: the neighbourhood is a 10 km x 10 km Lambertian plane with the TOC albedo of the forest. DART computes the TOC albedo of the forest and city for subzones (1 km × 1 km at city centre and 2 km × 2 km in top-left forest, in Figure 7).

Table 2. Atmosphere vertical scattering and absorption optical depth (OD), and city and forest TOC albedos, for four Sentinel-2A bands.

Band	Wavelength	Scattering OD	Absorption OD	City TOC albedo	Forest TOC albedo
B	0.4924 μm	0.501	0.030	0.06	0.03
G	0.5598 μm	0.392	0.058	0.07	0.07
R	0.6646 μm	0.286	0.036	0.010	0.03
NIR	0.8328 μm	0.189	0.045	0.100	0.42

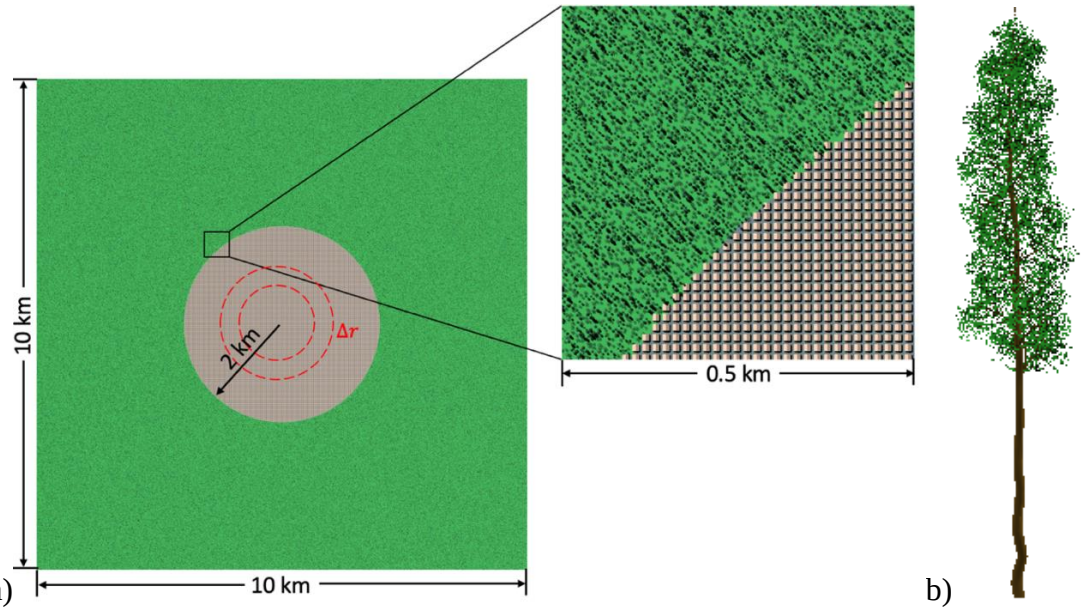

Figure 7. 3D case. a) Target: circular city of 2 km radius with 55828 houses spaced 15 m apart in a 10 × 10 km forest with 1553504 quasi-randomly distributed Tilia cordata trees at five growing stages, spaced ≈ 5 m apart). b) DART created house. b) Example of Tilia cordata: TICO 5.

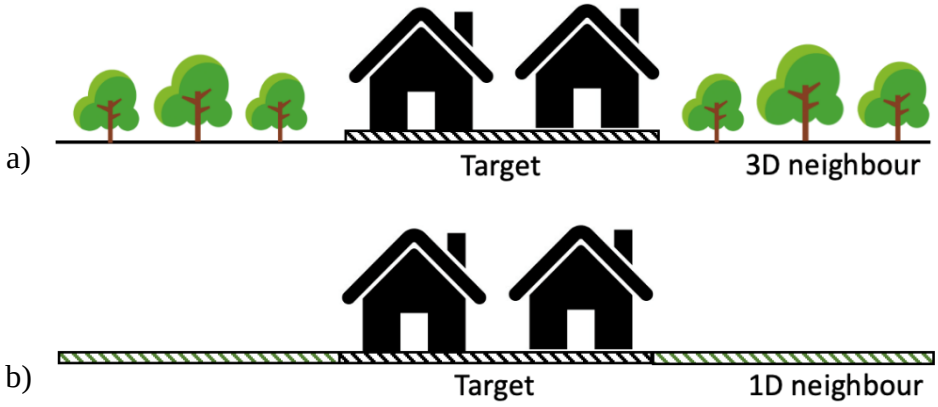

Figure 8. Two cases: city (*i.e.*, target) in a neighbourhood that is a forest (a: 3D case) or a Lambertian plane with the forest TOC albedo (b: 1D case). The two cases have the same background.

4.2.2 Adjacency effect on TOA nadir radiance

The adjacency effect is evaluated as the difference of two simulations, one with the 1D/3D neighbourhood and the background and the other one with the neighbourhood and background as flat black surfaces. Figure 9 shows the TOA nadir adjacency NIR radiance $L_{\mathrm{adj}}(x, y)$ and $L_{\mathrm{adj}}(r)$ of the city with 1D (a) and 3D (b) neighbourhood, with r the distance from the city

centre to the edge ($r = 2$ km). L_{adj} increases from the city centre. It is larger for the 3D neighbourhood than for the 1D neighbourhoods, although both have the same TOC albedo. This is mostly due to the forest anisotropic reflectance.

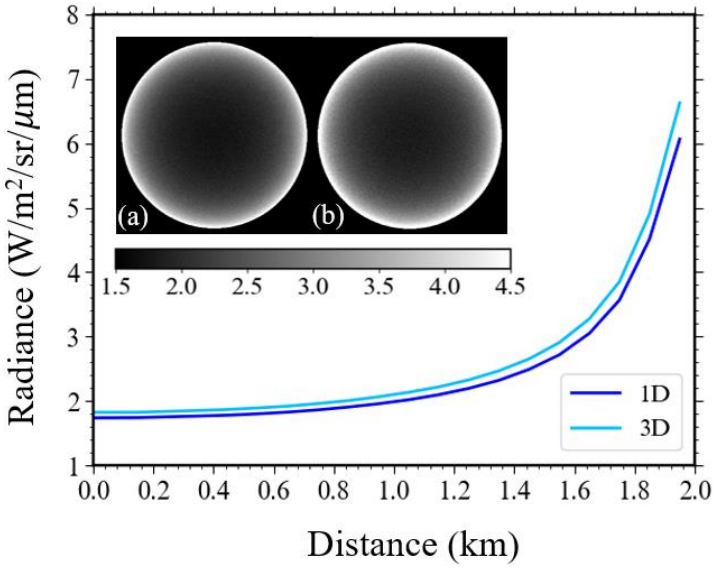

Figure 9. Adjacency radiance L_{adj} in the nadir TOA images for the 1D (a) and 3D (b) neighbourhoods at NIR band. $L_{\mathrm{adj}}(r)$ greatly increases with distance r from the city centre to the edge. $L_{\mathrm{adj}}(r)$ is the average for all pixels $L_{\mathrm{adj}}(x, y)$ in the ring $[r, r+\Delta r]$ with Δr=0.1 km (Table 3).

Table 3 shows nadir L_{adj} at city centre and edge, and its relative contribution $\zeta_{L_{\mathrm{adj}}} = L_{\mathrm{adj}}/L_{\mathrm{TOA}}$ to TOA radiance for four Sentinel-2A bands. L_{adj} is $\approx 2-3$ times larger at the edge of the city than at its centre, for all bands. It reaches ~20% in the NIR band. L_{adj} and $\zeta_{L_{\mathrm{adj}}}$ increase with the neighbour TOC albedo and the importance of atmospheric scattering. For example, $\zeta_{L_{\mathrm{adj}}}$ is more than 5 times larger in NIR band than in the red band because the forest TOC albedo is more than 12 times larger in the NIR band than in the red band. Also, $\zeta_{L_{\mathrm{adj}}}$ is more than 1.5 times larger in the blue band than in the red band, although the TOC albedo of the forest is similar, because the atmosphere scatters more in the blue band than in the red band (*cf.* atmospheric scattering optical depth in Table 2). The study of adjacency effect under different aerosol loadings in the Appendix C confirms this point. We also note that the impact of 3D

structure on the adjacency radiance is maximal in the NIR band, the $\zeta_{L_{\mathrm{adj}}}$ values of the 1D and 3D cases differ by 0.3% at the city centre and by 1.3% at the city edge.

Table 3. Adjacency radiance L_{adj} (W/m^2/sr/μm) and its relative contribution $\zeta_{L_{\mathrm{adj}}} = L_{\mathrm{adj}}/L_{\mathrm{TOA}}$ (%) to total TOA nadir radiance at the city centre and edge, for the four Sentinel-2A bands.

	1D neighbour				**3D neighbour**			
	Centre		Edge		Centre		Edge	
	L_{adj}	$\zeta_{L_{\mathrm{adj}}}$	L_{adj}	$\zeta_{L_{\mathrm{adj}}}$	L_{adj}	$\zeta_{L_{\mathrm{adj}}}$	L_{adj}	$\zeta_{L_{\mathrm{adj}}}$
B	1.4	2.2%	2.5	4.2%	1.4	2.3%	2.8	4.7%
G	1.8	3.6%	3.9	8.0%	1.9	3.9%	4.4	9.0%
R	0.4	0.9%	1.1	2.5%	0.4	1.0%	1.2	2.8%
NIR	1.7	5.5%	6.1	17.5%	1.8	5.8%	6.6	18.8%

4.2.3 Adjacency effect on directional radiance and albedo

The TOA albedo of the city centre and the edge are simulated using the BRF camera (Figure 2) in mode 3, for a user-defined plane (Δx=Δy=100 m) with altitude H=15 m, mode 3 to obtain the TOA signal and mode 1 to obtain the TOC signal. Figure 10 shows the directional distributions of TOA radiance L_{TOA}, adjacency radiance L_{adj} and its relative contribution $\zeta_{L_{\mathrm{adj}}}$, at the city centre and edge, for the NIR band. L_{TOA} tends to be larger in the backward directions due to the hot-spot effect of the 3D land surface and is smaller in the forward directions due to the observation of the shadows of the city buildings. L_{adj} increases with the obliquity of the observation directions. For example, $\zeta_{L_{\mathrm{adj}}}$ can be as high as 60% for directions with VZA = 80°, because increasing the "sensor-city" path (*i.e.*, larger atmospheric optical depth for observation) decreases the city signal and increases the city neighbourhood signal by atmospheric scattering.

TOA exitance M_{TOA} is the hemispherical integral of the directional average upward TOA radiance of a surface at TOC level. TOA albedo $\mathcal{A}_{TOA}$ is the ratio of TOA exitance M_{TOA} to TOA irradiance E_{TOA}. Table 4 shows the contribution $\mathcal{A}_{adj}^{Z}$ (altitude level Z can be TOC or TOA) due to the adjacency effect and its relative importance $\zeta_{\mathcal{A}_{adj}^{Z}} = \mathcal{A}_{adj}^{Z}/\mathcal{A}_{Z}$ at the city centre and edge, for the four Sentinel-2A bands. $\zeta_{\mathcal{A}_{adj}^{TOA}}$ is usually larger than 5%, the maximum TOC albedo uncertainty advised by the Global Climate Observing System (GCOS: https://gcos.wmo.int/en/essential-climate-variables/albedo/). Therefore, the adjacency effect can be a significant source of uncertainty for the interpretation of TOC albedo from RS images if they are not corrected by the atmospheric correction algorithm. Here, the large TOC albedo of the neighbour forest in the NIR can increase $\mathcal{A}_{adj}^{TOA}$ up to 0.035 (*i.e.*, 28.1% of the total TOA albedo). Although it impacts the directional radiance, the 3D structure of the neighbourhood only slightly influences $\mathcal{A}_{adj}^{TOA}$: the difference of $\mathcal{A}_{adj}^{TOA}$ between 1D and 3D neighbour case is less than 0.8% for all four bands.

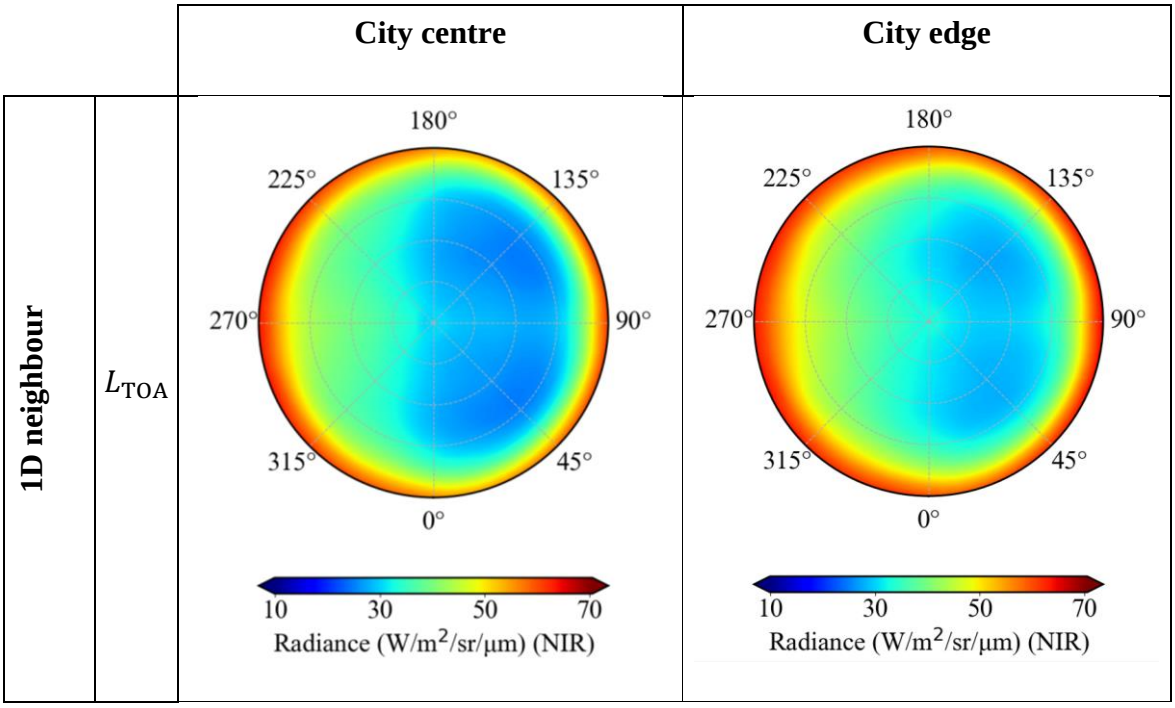

a)

		City centre	City edge
1D neighbour	L_{adj}	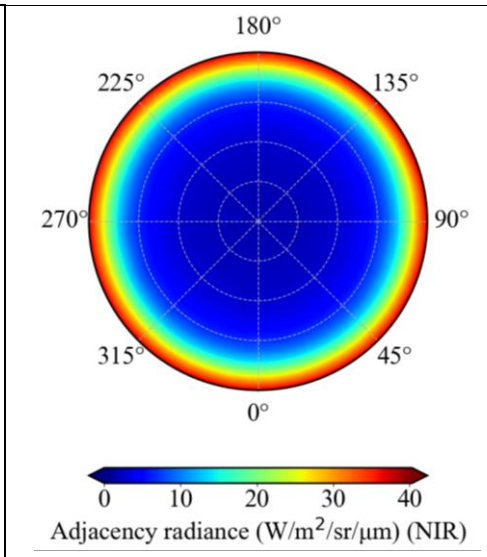	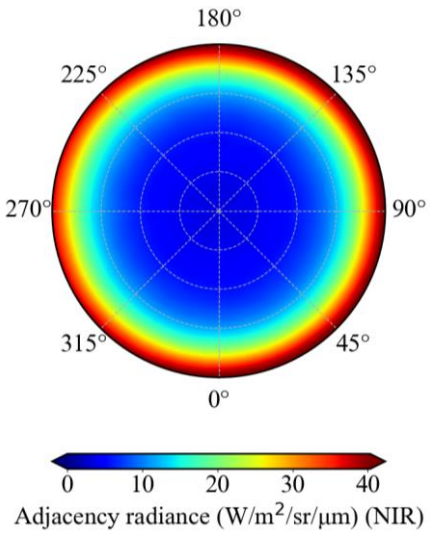
1D neighbour	$\zeta_{L_{\mathrm{adj}}}$	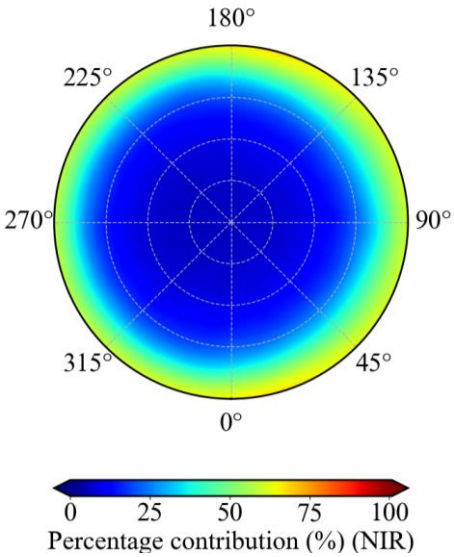	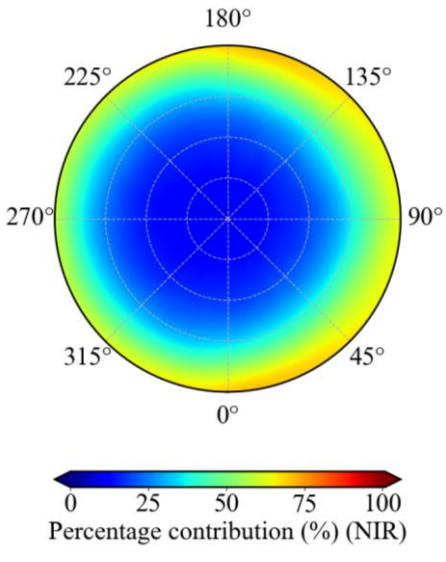

b)

3D neighbour	L_{TOA}	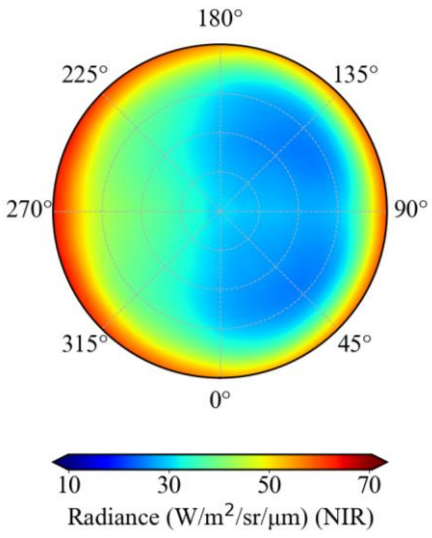	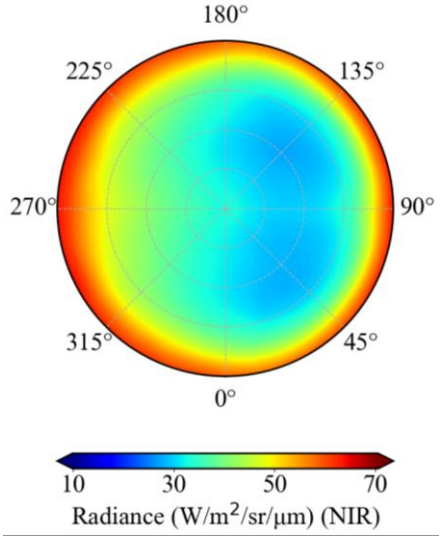
3D neighbour	L_{adj}	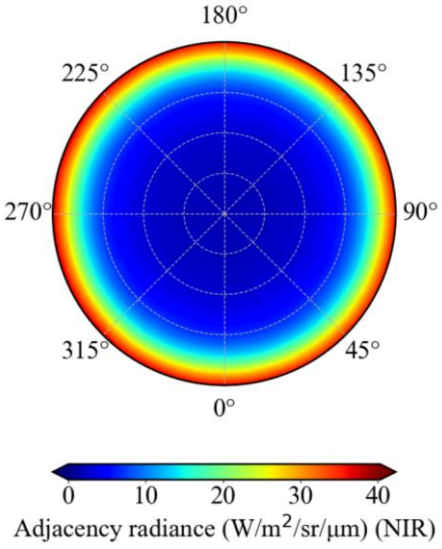	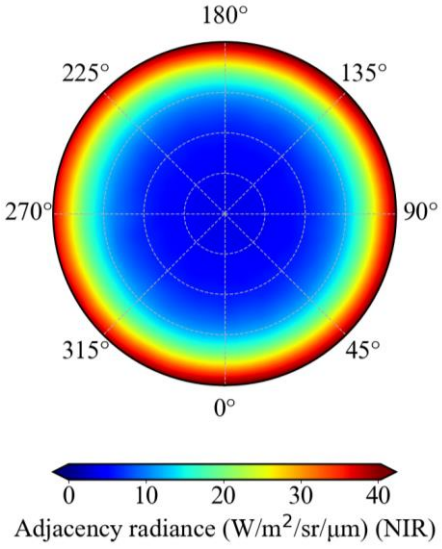
3D neighbour	$\zeta_{L_{\mathrm{adj}}}$	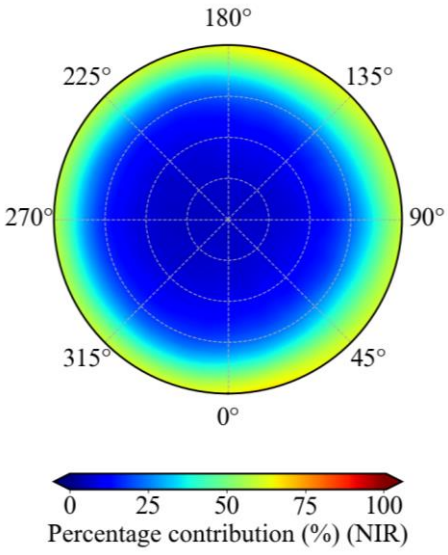	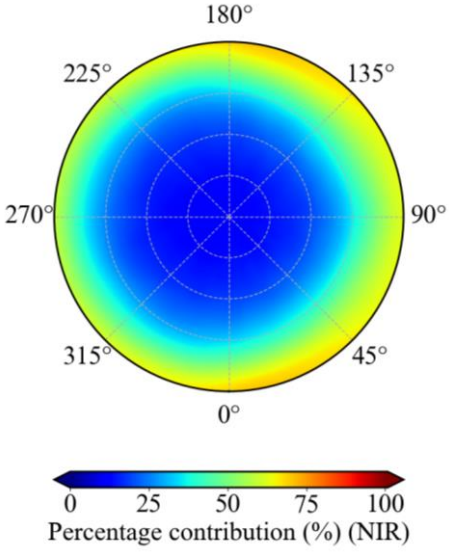

496

Figure 10. Angular plots of TOA total radiance L_{TOA}, radiance L_{adj} due to the adjacency effect, and relative contribution $\zeta_{L_{\mathrm{adj}}}$ at the city centre and edge. NIR band. a) 1D neighbour. b) 3D neighbour.

Table 4. Adjacency TOA albedo $\mathcal{A}_{\mathrm{adj}}^{\mathrm{TOA}}$ and its percentage contribution $\zeta_{\mathcal{A}_{\mathrm{adj}}^{\mathrm{TOA}}}=\mathcal{A}_{\mathrm{adj}}^{\mathrm{TOA}}/\mathcal{A}_{\mathrm{TOA}}$ (%) to total TOA albedo at the city centre and edge, for four Sentinel-2A bands.

	1D neighbour				**3D neighbour**			
	Centre		Edge		Centre		Edge	
	$\mathcal{A}_{\mathrm{adj}}^{\mathrm{TOA}}$	$\zeta_{\mathcal{A}_{\mathrm{adj}}^{\mathrm{TOA}}}$	$\mathcal{A}_{\mathrm{adj}}^{\mathrm{TOA}}$	$\zeta_{\mathcal{A}_{\mathrm{adj}}^{\mathrm{TOA}}}$	$\mathcal{A}_{\mathrm{adj}}^{\mathrm{TOA}}$	$\zeta_{\mathcal{A}_{\mathrm{adj}}^{\mathrm{TOA}}}$	$\mathcal{A}_{\mathrm{adj}}^{\mathrm{TOA}}$	$\zeta_{\mathcal{A}_{\mathrm{adj}}^{\mathrm{TOA}}}$
B	0.004	3.8%	0.006	4.9%	0.005	3.9%	0.007	5.2%
G	0.008	7.4%	0.010	10.1%	0.008	7.6%	0.011	10.6%
R	0.003	2.6%	0.004	3.9%	0.003	2.6%	0.004	4.1%
NIR	0.021	18.6%	0.033	27.3%	0.022	19.0%	0.035	28.1%

The influence of the adjacency effect is smaller on the TOC irradiance and TOC exitance than on the TOA exitance. Its relative contribution to local TOC albedo $\mathcal{A}_{\mathrm{TOC}}$ is even smaller because it contributes in a similar way to TOC exitance $\mathrm{M}_{\mathrm{TOC}}$ and irradiance $\mathrm{E}_{\mathrm{TOC}}$: it is only about 0.13% at NIR band, 0.01% at the red band, 0.03% at the green band and 0.03% at the blue band. Table 5 shows $\mathrm{M}_{\mathrm{TOC}}$, $\mathrm{E}_{\mathrm{TOC}}$ and $\mathcal{A}_{\mathrm{TOC}}$ at NIR band as well as their respective increases $\Delta_{\mathrm{adj}}^{\mathrm{TOC}}$ due to the adjacency effect, at the city centre and edge, for 1D and 3D neighbour cases. The ratio of the components $\Delta_{\mathrm{adj}}^{\mathrm{TOC}}$ to $\mathrm{M}_{\mathrm{TOC}}$ and $\mathrm{E}_{\mathrm{TOC}}$ is close to $\mathcal{A}_{\mathrm{TOC}}$ (*i.e.*, $\Delta_{\mathrm{adj}}^{\mathrm{M_{TOC}}}/\Delta_{\mathrm{adj}}^{\mathrm{E_{TOC}}}\approx\mathcal{A}_{\mathrm{TOC}}$).

Table 5. TOC exitance M_{TOC} (W/m^2/μm), irradiance E_{TOC} (W/m^2/μm) and albedo $\mathcal{A}_{TOC}$ at NIR band as well as their component Δ_{adj}^{TOC} due to the adjacency effect. E_{TOC} is the integral of directional radiance captured by a fisheye camera looking upward and placed at the city centre and edge.

	1D neighbour				**3D neighbour**			
	Centre		Edge		Centre		Edge	
	Total	Δ_{adj}^{TOC}	Total	Δ_{adj}^{TOC}	Total	Δ_{adj}^{TOC}	Total	Δ_{adj}^{TOC}
M_{TOC}	87.67	0.92	87.87	1.06	87.67	0.91	87.88	1.07
E_{TOC}	857.99	8.90	858.24	9.26	858.03	8.94	858.33	9.35
$\mathcal{A}_{TOC}$	0.1022	0.0000	0.1024	0.0001	0.1022	0.0000	0.1024	0.0001

5 Concluding remarks

This paper presents the new 3D Monte Carlo modelling of surface-atmosphere RT in DART as an extension and adaptation of the initial light transport theory to scenes that comprise surfaces and volumes. It also presents a new Earth-Atmosphere system. It is designed to simulate accurate remote sensing observations and their atmospheric contributions, including those due to the adjacency effect. The default setting of this Earth-Atmosphere system (*i.e.*, X × Y × Z = 500 km × 500 km × 50 km) is consistent (relative error < 0.1%) with a quasi-infinite parallel atmosphere. Its dimensions can be easily adapted to any experimental context. Its atmospheric RT modelling has been successfully evaluated with SMART-G with an atmosphere defined in the IPRT program. The relative root mean square difference of TOA reflectance is 0.20% for 629 upward viewing directions from VZA = 0° to 80° for infinite black surface, and 0.03% for the points on the radius of a black disc inside infinite white environment. These differences are mainly due to Monte Carlo noise and the roundoff error of computing.

This new DART modelling is very well adapted to study the influence of the adjacency effect on remotely sensed radiance of land surfaces at any altitude. We studied this influence for a scene made up of a target city (radius 2 km) surrounded by a forest (dimension 10 km), for four Sentinel-2A bands (blue, green, red, NIR). Results allow one to quantify the increase of the adjacency effect with larger TOC albedo of the neighbouring forest and atmospheric scattering. In our experiment, the adjacency effect contributes up to ~ 5.5% at the city centre and up to ~20% at the city edge to the TOA nadir NIR radiance, which is more than 5 times larger than that at red band (~1% at the city centre and ~3% at the city edge). It is explained by the fact that the forest TOC albedo at NIR band is more than 12 times larger than in the red band. The adjacency effect in the blue band is 1.5 times larger than that of the red band at the city centre and edge although forest TOC albedo is similar in the blue and red bands, because the atmosphere scatters more in the blue band than in the red band. The 3D structure of the neighbouring forest also plays a role because it drives the angular distribution of the radiation scattered by the neighbourhood of the city. Compared to the 1D Lambertian neighbour case, it can induce a difference of adjacency contribution up to 1.3% for the edge of the city for the NIR band.

The BRF camera of DART has been adapted to the new Earth-Atmosphere system in order to simulate the hemispherical distribution of the upward radiance, then to compute the corresponding albedo at a given altitude, a key parameter reflecting the radiative balance. Results show that the adjacency contribution increases if the observing direction is more inclined. In our virtual experiment, at observing zenith equal to 80°, the adjacency contribution in the NIR band can represent up to 60% of the TOA radiance. The increased TOA albedo due to adjacency effect for the four Sentinel-2A bands considered is generally larger than the required maximum TOC albedo uncertainty 5% in applications as reported in GCOS. For

example, the proportion of adjacency albedo in total TOA albedo can reach 10% in the green band and 27% in the NIR band. The anisotropic reflectance of the forest that surrounds the city influences the TOA radiance of the city, but only slightly influences the TOA albedo of the city. The adjacency effect changes TOC irradiance but hardly changes the TOC albedo since the adjacency effect increases both the TOC irradiance and exitance.

This work expands the potential of DART to study and correct atmospheric effects in remote sensing images through the consideration of realistic landscapes with their spatial heterogeneity, 3D architecture, topography, *etc*. It also helps quantifying the error in the fast methods that estimate approximately the adjacency effect.

Acknowledgement

This work is funded by the Région Occitanie, France, the Paul Sabatier University, and the TOSCA program of the French Space Agency (CNES).

Appendix A. The default atmosphere dimension

The default parameters (*e.g.*, 50 km altitude, 500 km × 500 km atmosphere horizontal dimension) of the new Earth - Atmosphere system (*cf.* section 3.1) were derived from sensitivity studies in order to be optimal in usual configurations. For example, larger dimensions improve accuracy but increase simulation time. The optimal altitude was determined using MODTRAN as a reference. Considered an atmosphere characterized by the USSTD76 gas model and the Rural aerosol model, TOC albedo equal to 0.5, 2721 bands from 0.32 to 2.5 μm, nadir solar and viewing directions, and sensors at 40 km, 45 km, 50 km, 55 km, 60 km and 70 km altitudes. The relative differences ε between sensor and MODTRAN spectra are very small and decrease with altitude (Figure A.1, Table A.1). For the selected 50 km altitude ε = 0.07%.

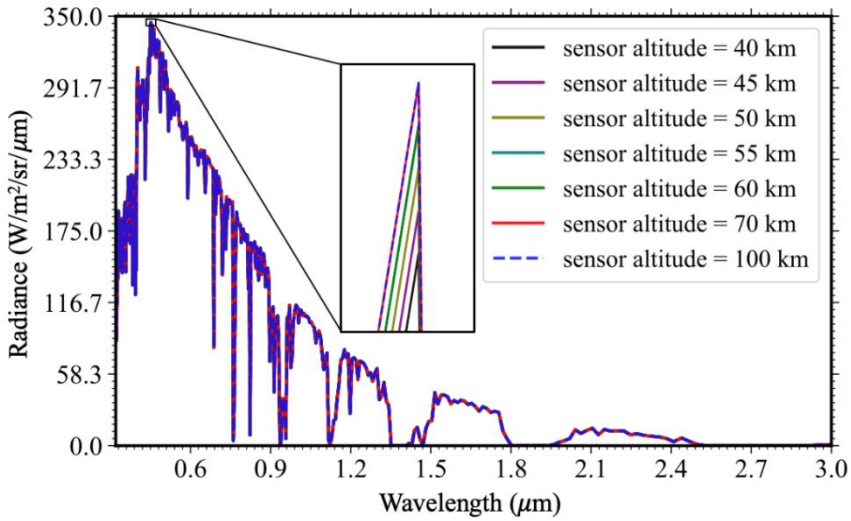

Figure A.1. MODTRAN TOA radiance spectra at seven sensor altitudes (40 km, 45 km, 50 km, 55 km, 60 km, 70 km, 100 km). TOC albedo is 0.5. USSTD76 atmosphere model with rural aerosols.

Table A.1. Mean relative error ε of radiance spectra at six sensor altitudes (Figure A.1) compared to the reference radiance spectrum of a sensor at 100 km altitude.

Sensor altitude	40 km	45 km	50 km	55 km	60 km	70 km
ε	0.17%	0.07%	0.07%	0.06%	0.03%	0.01%

The optimal horizontal dimension D_{XY} of the atmosphere volume was studied using a DART simulation with D_{XY} = 10000 km as a reference, for a TOC albedo equal to 0.5, an atmosphere characterized by the USSTD76 gas model and rural aerosol model, and nadir solar and viewing directions. D_{XY} was set to 20 km, 50 km, 100 km, 200 km, 500 km, and 10000 km. Figure A.2 shows that a small D_{XY} value *(e.g.*, 20 km) leads to a large underestimate of TOA reflectance in the visible domain. Table A.2 shows the average relative error ε for each D_{XY} value. D_{XY} = 500 km is a good approximation for an infinite parallel atmosphere because ε=0.08%.

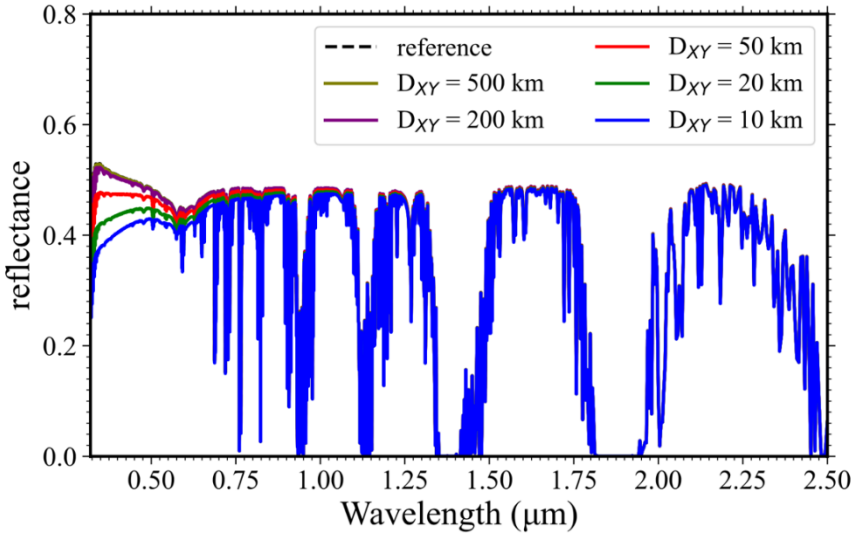

Figure A.2. DART TOA nadir reflectance for five atmosphere horizontal dimensions D_{XY} (20 km, 50 km, 100 km, 200 km, 500 km). TOC albedo is 0.5. USSTD76 atmosphere model with rural aerosols. The reference is for D_{XY}=10000 km.

Table A.2. The mean relative error ε of all DART TOA nadir reflectance spectra (Figure A.2) compared to the reference spectrum simulated with D_{XY} = 10000 km.

D_{XY}	20 km	50 km	100 km	200 km	500 km
ε	7.74%	3.59%	0.55%	0.45%	0.08%

Appendix B. Radiance estimate for a semi-infinite atmosphere

For the semi-infinite plane-parallel atmosphere, illuminated by parallel sunlight and observed by an orthographic camera, the radiance estimate $F_{\mathrm{IS}}^{(j)} = \sum_{n=1}^{\infty} \left[\frac{\tilde{L}_e(r_n \to r_{n-1}) \cdot \tilde{G}(r_0 \leftrightarrow r_1) \cdot W_e^{(j)}(r_0 \to r_1)}{\overleftarrow{p}(r_0) \cdot \overleftarrow{p}(r_1)} \cdot \prod_{k=2}^{n} \frac{\tilde{f}_s(r_k \to r_{k-1} \to r_{k-2}) \cdot \tilde{G}(r_{k-1} \leftrightarrow r_k)}{\overleftarrow{p}(r_k)} \right]$ (Eq. (23)) can be simplified since all vertices, except those at the light source and sensor, are in the medium, we have:

$$\frac{\tilde{G}(r_0 \leftrightarrow r_1) \cdot W_e^{(j)}(r_0 \to r_1)}{\overleftarrow{p}(r_0) \cdot \overleftarrow{p}(r_1)} = \frac{\mathcal{T}(r_0 \leftrightarrow r_1) \cdot \frac{\cos\theta_i^{r_0}}{\|r_0 - r_1\|^2} \cdot \frac{\delta(\Omega_0 - \Omega_{\mathrm{d}})}{A_{\mathrm{img}}}}{\frac{1}{A_{\mathrm{img}}} \cdot \frac{\delta(\Omega_0 - \Omega_{\mathrm{d}})}{\|r_0 - r_1\|^2} \cdot \alpha_e(r_0 \to r_1) \cdot \mathcal{T}(r_0 \leftrightarrow r_1)} = \frac{1}{\alpha_e(r_0 \to r_1)}$$

$$\frac{\tilde{f}_s(r_k \to r_{k\text{-}1} \to r_{k\text{-}2}) \cdot \tilde{G}(r_{k\text{-}1} \leftrightarrow r_k)}{\overleftarrow{p}(r_k)} = \frac{\alpha_s(r_k \to r_{k\text{-}1}) \cdot \frac{P(r_k \to r_{k\text{-}1} \to r_{k\text{-}2})}{4\pi} \cdot \frac{\mathcal{T}(r_{k\text{-}1} \leftrightarrow r_k)}{\|r_{k\text{-}1} - r_k\|^2}}{\frac{P(r_k \to r_{k\text{-}1} \to r_{k\text{-}2})}{4\pi} \cdot \frac{\alpha_e(r_{k\text{-}1} \to r_k) \cdot \mathcal{T}(r_{k\text{-}1} \leftrightarrow r_k)}{\|r_{k\text{-}1} - r_k\|^2}} = \frac{\alpha_s(r_k \to r_{k\text{-}1})}{\alpha_e(r_{k\text{-}1} \to r_k)}$$

Besides, the direct connection of the light source indicates:

$$\frac{\tilde{L}_e(r_n \to r_{n-1}) \cdot \tilde{f}_s(r_n \to r_{n-1} \to r_{n-2}) \cdot \tilde{G}(r_{n-1} \leftrightarrow r_n)}{\overleftarrow{p}(r_n)}$$

$$= \frac{E_s \cdot \delta(\Omega_{n-1} - \Omega_s) \cdot \alpha_s(r_n \to r_{n-1}) \cdot \frac{P(r_n \to r_{n-1} \to r_{n-2})}{4\pi} \cdot \frac{\mathcal{T}(r_{n-1} \leftrightarrow r_n)}{\|r_{n-1} - r_n\|^2}}{\delta(\Omega_{n-1} - \Omega_s) \cdot \frac{\cos\theta_o^{r_n}}{\|r_{n-1} - r_n\|^2}}$$

$$= E_s \cdot \alpha_s(r_n \to r_{n-1}) \cdot \mathcal{T}(r_{n-1} \leftrightarrow r_n) \cdot \frac{P(r_n \to r_{n-1} \to r_{n-2})}{4\pi}$$

with E_s the solar constant at TOA, and Ω_s the solar direction.

Assuming that atmospheric constituents are isotropic, extinction coefficients depend only on location. After a few mathematical manipulations, we obtain a form consistent with the SSA method in (Spada et al., 2006):

$$F_{\mathrm{IS}}^{(j)} = \sum_{n=1}^{\infty} \left[E_s \cdot \mathcal{T}(r_n \leftrightarrow r_{n-1}) \cdot \frac{P(r_n \to r_{n-1} \to r_{n-2})}{4\pi} \cdot \prod_{k=1}^{n-1} \frac{\alpha_s(r_k)}{\alpha_e(r_k)} \right]$$

Appendix C. Adjacency effect under different aerosol loadings

The adjacency effect is mostly due to scene elements at short distance if the aerosol optical depth (AOD) is high, and at greater distances if the AOD is small (Houborg and McCabe, 2016). Here, we consider TOA reflectance for different AODs. The scene is a black disc with radius equal to 2 km surrounded by an infinite white environment. The atmosphere is characterized by a USSTD76 gas model and a Rural aerosol model. SZA = 30° and SAA = 270°. Figure C.1 shows the TOA adjacency reflectance of the disc as a function of distance from the disc centre to edge for four different AODs. The AOD in DART was scaled by a so-called multiplicative factor applied to the aerosol vertical profile. For example, a factor equal to 0.5 means the resulted AOD is the AOD of Rural aerosol model multiplied by 0.5. Four factors were considered: 0, 0.5, 1 and 5. Figure C.1 shows that the adjacency effect decreases at the disc centre if AOD increases. The trend is more complex on the disc border: an AOD increase leads to an increase of the adjacency effect if AOD is low (i.e., factor less or equal to 1), and to a decrease of the adjacency effect if the AOD is very high (i.e., factor 5).

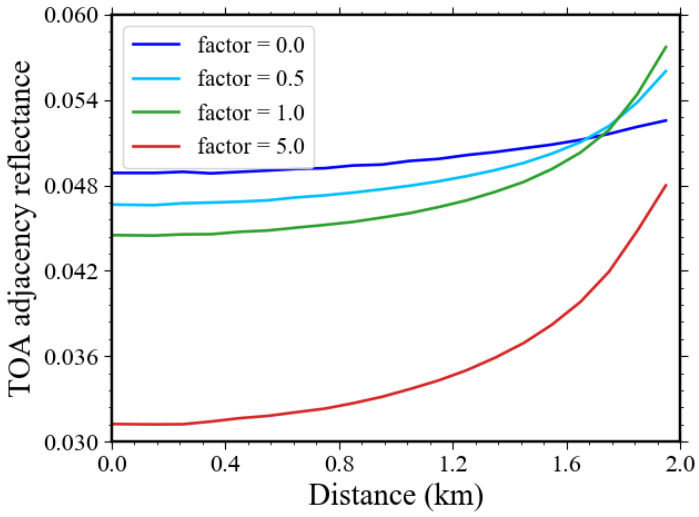

Figure C.1. TOA adjacency reflectance from the centre to border of the black disc, for four different aerosol loadings.

Reference

Adler-Golden, S.M., Matthew, M.W., Berk, A., Fox, M.J., Lee, J., Ratkowski, A.J., 2008. Improvements in aerosol retrieval for atmospheric correction, in: IGARSS 2008-2008 IEEE International Geoscience and Remote Sensing Symposium. IEEE, pp. III–130.

Amanatides, J., Woo, A., 1987. A fast voxel traversal algorithm for ray tracing., in: Eurographics. pp. 3–10.

Anderson, G.P., Clough, S.A., Kneizys, F.X., Chetwynd, J.H., Shettle, E.P., 1986. AFGL atmospheric constituent profiles (0.120 km). AIR FORCE GEOPHYSICS LAB HANSCOM AFB MA.

Bablet, A., Vu, P.V.H., Jacquemoud, S., Viallefont-Robinet, F., Fabre, S., Briottet, X., Sadeghi, M., Whiting, M.L., Baret, F., Tian, J., 2018. MARMIT: A multilayer radiative transfer model of soil reflectance to estimate surface soil moisture content in the solar domain (400–2500 nm). Remote Sens Environ 217, 1–17.

Barlakas, V., Macke, A., Wendisch, M., 2016. SPARTA–solver for polarized atmospheric radiative transfer applications: introduction and application to Saharan dust fields. J Quant Spectrosc Radiat Transf 178, 77–92.

Bates, D.R., 1984. Rayleigh scattering by air. Planet Space Sci 32, 785–790.

Berk, A., Hawes, F., 2017. Validation of MODTRAN® 6 and its line-by-line algorithm. J Quant Spectrosc Radiat Transf 203, 542–556.

Borel, C.C., Gerstl, S.A.W., 1992. Adjacency-blurring effect of scenes modeled by the radiosity method, in: Atmospheric Propagation and Remote Sensing. International Society for Optics and Photonics, pp. 620–624.

Bucholtz, A., 1995. Rayleigh-scattering calculations for the terrestrial atmosphere. Appl Opt 34, 2765–2773.

Bulgarelli, B., Zibordi, G., 2018. On the detectability of adjacency effects in ocean color remote sensing of mid-latitude coastal environments by SeaWiFS, MODIS-A, MERIS, OLCI, OLI and MSI. Remote Sens Environ 209, 423–438.

Cornet, C., C-Labonnote, L., Szczap, F., 2010. Three-dimensional polarized Monte Carlo atmospheric radiative transfer model (3DMCPOL): 3D effects on polarized visible reflectances of a cirrus cloud. J Quant Spectrosc Radiat Transf 111, 174–186.

Dave, J. V, 1980. Effect of atmospheric conditions on remote sensing of a surface nonhomogeneity. Photogramm Eng Remote Sensing 46, 1173–1180.

Dupiau, A., Jacquemoud, S., Briottet, X., Fabre, S., Viallefont-Robinet, F., Philpot, W., Di Biagio, C., Hébert, M., Formenti, P., 2022. MARMIT-2: An improved version of the MARMIT model to predict soil reflectance as a function of surface water content in the solar domain. Remote Sens Environ 272, 112951.

Emde, C., Barlakas, V., Cornet, C., Evans, F., Korkin, S., Ota, Y., Labonnote, L.C., Lyapustin, A., Macke, A., Mayer, B., 2015. IPRT polarized radiative transfer model intercomparison project–Phase A. J Quant Spectrosc Radiat Transf 164, 8–36.

Farin, G., 2014. Curves and surfaces for computer-aided geometric design: a practical guide. Elsevier.

Féret, J.-B., Gitelson, A.A., Noble, S.D., Jacquemoud, S., 2017. PROSPECT-D: Towards modeling leaf optical properties through a complete lifecycle. Remote Sens Environ 193, 204–215.

Gascon, F., Gastellu-Etchegorry, J.-P., Lefèvre, M.-J., 2001. Radiative transfer model for simulating high-resolution satellite images. IEEE Transactions on Geoscience and Remote Sensing 39, 1922–1926.

Gastellu-Etchegorry, J.-P., Demarez, V., Pinel, V., Zagolski, F., 1996. Modeling radiative transfer in heterogeneous 3-D vegetation canopies. Remote Sens Environ 58, 131–156.

688 Govaerts, Y.M., Jacquemoud, S., Verstraete, M.M., Ustin, S.L., 1996. Three-dimensional
689 radiation transfer modeling in a dicotyledon leaf. Appl Opt 35, 6585–6598.
690 Grau, E., Gastellu-Etchegorry, J.-P., 2013. Radiative transfer modeling in the Earth–
691 Atmosphere system with DART model. Remote Sens Environ 139, 149–170.
692 Houborg, R., McCabe, M.F., 2016. Adapting a regularized canopy reflectance model
693 (REGFLEC) for the retrieval challenges of dryland agricultural systems. Remote Sens
694 Environ 186, 105–120.
695 Jacquemoud, S., Baret, F., 1990. PROSPECT: A model of leaf optical properties spectra.
696 Remote Sens Environ 34, 75–91.
697 Kiselev, V., Bulgarelli, B., Heege, T., 2015. Sensor independent adjacency correction algorithm
698 for coastal and inland water systems. Remote Sens Environ 157, 85–95.
699 Landier, L., Gastellu-Etchegorry, J.P., Al Bitar, A., Chavanon, E., Lauret, N., Feigenwinter, C.,
700 Mitraka, Z., Chrysoulakis, N., 2018. Calibration of urban canopies albedo and 3D
701 shortwave radiative budget using remote-sensing data and the DART model. Eur J Remote
702 Sens 51, 739–753. https://doi.org/10.1080/22797254.2018.1462102
703 Lewis, P., 1999. Three-dimensional plant modelling for remote sensing simulation studies
704 using the Botanical Plant Modelling System. Agronomie 19, 185–210.
705 Liang, S., Fang, H., Chen, M., 2001. Atmospheric correction of Landsat ETM+ land surface
706 imagery. I. Methods. IEEE Transactions on geoscience and remote sensing 39, 2490–2498.
707 Mekler, Y., Kaufman, Y.J., 1980. The effect of Earth's atmosphere on contrast reduction· for a
708 nonuniform surface albedo and 'two-halves' field. J Geophys Res Oceans 85, 4067–4083.
709 Miesch, C., Poutier, L., Achard, V., Briottet, X., Lenot, X., Boucher, Y., 2005. Direct and
710 inverse radiative transfer solutions for visible and near-infrared hyperspectral imagery.
711 IEEE Transactions on Geoscience and Remote Sensing 43, 1552–1562.

Minomura, M., Kuze, H., Takeuchi, N., 2001. Atmospheric correction of visible and near-infrared satellite data using radiance components: an improved treatment of adjacency effect. Journal of the Remote Sensing Society of Japan 21, 260–271.

Mishchenko, M.I., Travis, L.D., Lacis, A.A., 2006. Multiple scattering of light by particles: radiative transfer and coherent backscattering. Cambridge University Press.

Ouaidrari, H., Vermote, E.F., 1999. Operational atmospheric correction of Landsat TM data. Remote Sens Environ 70, 4–15.

Pan, Y., Bélanger, S., Huot, Y., 2022. Evaluation of atmospheric correction algorithms over lakes for high-resolution multispectral imagery: Implications of adjacency effect. Remote Sens (Basel) 14, 2979.

Pearce, W.A., 1986. Monte Carlo study of the atmospheric spread function. Appl Opt 25, 438–447.

Petty, G.W., 2006. A first course in atmospheric radiation. Sundog Pub.

Qi, J., Xie, D., Yin, T., Yan, G., Gastellu-Etchegorry, J.-P., Li, L., Zhang, W., Mu, X., Norford, L.K., 2019. LESS: LargE-Scale remote sensing data and image simulation framework over heterogeneous 3D scenes. Remote Sens Environ 221, 695–706.

Ramon, D., Steinmetz, F., Jolivet, D., Compiègne, M., Frouin, R., 2019. Modeling polarized radiative transfer in the ocean-atmosphere system with the GPU-accelerated SMART-G Monte Carlo code. J Quant Spectrosc Radiat Transf 222, 89–107.

Regaieg, O., 2023. Modélisation du transfert radiatif de la fluorescence induite par le soleil, de l'émission thermique et du bilan radiatif des couverts végétaux 3D: vers un modèle SIF complet.

Reinersman, P.N., Carder, K.L., 1995. Monte Carlo simulation of the atmospheric point-spread function with an application to correction for the adjacency effect. Appl Opt 34, 4453–4471.

Richter, R., 1990. A fast atmospheric correction algorithm applied to Landsat TM images. TitleREMOTE SENSING 11, 159–166.

Rubinstein, R.Y., Kroese, D.P., 2016. Simulation and the Monte Carlo method. John Wiley & Sons.

Santer, R., Schmechtig, C., 2000. Adjacency effects on water surfaces: primary scattering approximation and sensitivity study. Appl Opt 39, 361–375.

Shettle, E.P., Fenn, R.W., 1979. Models for the aerosols of the lower atmosphere and the effects of humidity variations on their optical properties. Optical Physics Division, Air Force Geophysics Laboratory.

Spada, F., Krol, M.C., Stammes, P., 2006. McSCIA: application of the Equivalence Theorem in a Monte Carlo radiative transfer model for spherical shell atmospheres. Atmos Chem Phys 6, 4823–4842.

Sterckx, S., Knaeps, S., Kratzer, S., Ruddick, K., 2015. SIMilarity Environment Correction (SIMEC) applied to MERIS data over inland and coastal waters. Remote Sens Environ 157, 96–110.

Sun, B., Schäfer, M., Ehrlich, A., Jäkel, E., Wendisch, M., 2021. Influence of atmospheric adjacency effect on top-of-atmosphere radiances and its correction in the retrieval of Lambertian surface reflectivity based on three-dimensional radiative transfer. Remote Sens Environ 263, 112543.

Veach, E., Guibas, L.J., 1997. Metropolis light transport, in: Proceedings of the 24th Annual Conference on Computer Graphics and Interactive Techniques. pp. 65–76.

Vermote, E.F., Tanré, D., Deuze, J.L., Herman, M., Morcette, J.-J., 1997. Second simulation of the satellite signal in the solar spectrum, 6S: An overview. IEEE transactions on geoscience and remote sensing 35, 675–686.

Vilfan, N., Van der Tol, C., Muller, O., Rascher, U., Verhoef, W., 2016. Fluspect-B: A model for leaf fluorescence, reflectance and transmittance spectra. Remote Sens Environ 186, 596–615.

Wang, Y., Gastellu-Etchegorry, J.-P., 2021. Accurate and fast simulation of remote sensing images at top of atmosphere with DART-Lux. Remote Sens Environ 256. https://doi.org/10.1016/j.rse.2021.112311

Wang, Y., Gastellu-Etchegorry, J.-P., 2020. DART: Improvement of thermal infrared radiative transfer modelling for simulating top of atmosphere radiance. Remote Sens Environ 251, 112082.

Wang, Y., Kallel, A., Yang, X., Regaieg, O., Lauret, N., Guilleux, J., Chavanon, E., Gastellu-Etchegorry, J.-P., 2022. DART-Lux: An unbiased and rapid Monte Carlo radiative transfer method for simulating remote sensing images. Remote Sens Environ 274, 112973.

Wang, Y., Lauret, N., Gastellu-Etchegorry, J.-P., 2020. DART radiative transfer modelling for sloping landscapes. Remote Sens Environ. https://doi.org/10.1016/j.rse.2020.111902

Widlowski, J., Taberner, M., Pinty, B., Bruniquel-Pinel, V., Disney, M., Fernandes, R., Gastellu-Etchegorry, J., Gobron, N., Kuusk, A., Lavergne, T., 2007. Third Radiation Transfer Model Intercomparison (RAMI) exercise: Documenting progress in canopy reflectance models. Journal of Geophysical Research: Atmospheres 112.

Yin, T., Gastellu-Etchegorry, J.-P., Lauret, N., Grau, E., Rubio, J., 2013. A new approach of direction discretization and oversampling for 3D anisotropic radiative transfer modeling. Remote Sens Environ 135, 213–223.

Young, A.T., 1980. Revised depolarization corrections for atmospheric extinction. Appl Opt 19, 3427–3428.